Heterogeneous brittle-ductile deformation at shallow crustal levels under high thermal conditions: The case of a synkinematic contact aureole in inner northern Apennines, southeastern Elba Island, Italy

S. Papeschi[(1-2)], G. Musumeci[(2-3)], F. Mazzarini[(3)]

(1) Dipartimento di Scienze della Terra, Firenze University, Firenze, Italy

(2) Dipartimento di Scienze della Terra, Pisa University, Pisa, Italy

(3) Istituto Nazionale di Geofisica e Vulcanologia, Pisa, Italy

Abstract

We present an example of interaction between magmatism and tectonics at shallow crustal levels. In the Late Miocene the metamorphic units of the eastern Elba Island (northern Apennines) were intruded at very shallow crustal levels by a large pluton (>60 km^2) with the development of an hectometre-sized contact aureole defined by growth of low-pressure/high-temperature mineral assemblages (P_{max}<0.2 GPa, T_{max}~ 650°C). Structural data show that the contact aureole is associated with a km-sized antiform of the foliation and by several metre- to decametre-thick high-strain domains consisting of strongly foliated rocks containing synkinematic HT/LP mineral assemblages and ductile shear zones of variable thickness. These shear zones are characterized by a mylonitic foliation variably overprinted by cataclasis. Quartz microfabrics indicate that the dynamic crystallization processes progressively changed from grain boundary migration, associated with the thermal peak of contact metamorphism, to subgrain rotation and bulging recrystallization, the latter mostly associated with the cataclastic overprint. These transitions of recrystallization mechanisms in quartz are related to a progressive decrease of temperature during deformation. Deformation accompanied the development and cooling of the contact aureole, which recorded the switch from high temperature ductile to low temperature brittle conditions. The geometry of the studied deformation structures is consistent with the constraints of the regional tectonic evolution and its local interaction with the localized and transient thermal anomaly related to the coeval emplacement of igneous rocks.

Keywords: upper crust, contact aureole, heterogeneous deformation, ductile-brittle shear zones, quartz microfabric, Elba Island.

Corresponding author:

S. Papeschi, Dipartimento di Scienze della Terra, Pisa Università di Pisa, Via S. Maria, 53, 56126 Pisa, Italy.

e-mail: samuele.papeschi@unifi.it

1. Introduction

Contact aureoles are the result of heat, mass and mechanical energy provided to crustal rocks by magmatic intrusions. An interesting way to view contact aureoles is as gradients of temperature and strain between a pluton and its country rocks (Paterson et al., 1991a). The distribution of these gradients provides us with invaluable clues about the evolution of the plutonic system and the interaction between regional deformation and contact metamorphism.

Deformation in aureoles may reflect (i) the local strain field related to the magma emplacement in the host rock (forceful intrusion) and/or (ii) the effects of active regional deformation (tectonically-assisted intrusion). These represent "end-member" terms and in natural aureoles the total stress field likely is the combination of regional- and magma emplacement induced-stresses. Therefore, in contact aureoles evidences of pre-, syn- or post-thermal anomaly deformation may be preserved (Paterson et al., 1991b) making it difficult to separate and decipher both the background tectonic history and the processes that acted during pluton emplacement. The term “syn-tectonic” should therefore be restricted to contact aureoles and related intrusions containing unambiguous evidence that the "regional deformation" was coeval with magma emplacement and was active on the rocks being intruded by the magma (e.g. Paterson et al., 1991a, b).

The effects of magma emplacement and syntectonic processes on the fabrics of contact aureoles have been thoroughly documented in the middle and lower crust of several orogenic belts, as, for example, the Archean-Proterozoic belts (Karlstrom and Williams, 1995; Collins and Sawyer, 1996; Benn et al., 1998), Paleozoic belts (Hannula et al., 1999) and Mesozoic magmatic arcs (Paterson et al., 1991b). They remain, instead, still poorly documented in the upper brittle crust, where only a few cases are reported e.g., the Eureka-Joshua Flat-Beer Creek pluton (Nabelek and Morgan, 2012; Morgan et al., 2013) and the Adamello pluton (John and Blundy, 1993; Stipp et al., 2004).

In this paper, we describe the deformation structures recorded in the contact aureole of the Porto Azzurro Pluton of the northern Apennines, Italy, a buried intrusion (~60 km^2; Musumeci and Vaselli, 2012) of Upper Miocene age emplaced at very shallow (<0.2 GPa) crustal levels within an active collisional orogen. The contact aureole represents an example of interaction between regional deformation and a transient-thermal anomaly leading to a heterogeneous distribution of ductile and brittle structures in the host rocks. The analysis of quartz microfabrics indicates that ductile-brittle transition, mainly controlled by temperature decrease, occurred during continuous deformation. Overall, deformation was controlled by the background tectonic framework and continued once the Upper Miocene thermal pulse associated with pluton emplacement had faded away.

2. Geological Outline

2.1 The northern Apennines

The northern Apennines (Fig. 1a) are a NW-SE trending Cenozoic collisional belt belonging to the Alpine system. They formed from the Cretaceous-Eocene subduction of the Ligurian-Tethys Ocean and the following continental collision between the Adria plate and Europe (Corsica) (e.g. Boccaletti et al., 1971). The Oligocene to present history of the northern Apennines was marked by the progressive westward underthrusting of the Adriatic lithosphere (Adria plate) and the northeastward migration of the thrust front towards the Adriatic–Po Plain foreland. The structure of the northern Apennines (Elter, 1975) is characterized, from top to bottom (Fig. 1a), by: 1) non metamorphic ocean-derived units (Ligurian Units s.l.), 2) anchizonal cover nappes of the Triassic-Oligocene Adria continental passive margin sequences (Tuscan Nappe, TN) and 3) low metamorphic grade continental basement and cover nappes (Tuscan Metamorphic Units, TMUs). On the external (Adriatic) side, the northern Apennines are characterized by non-metamorphic units (external Cervarola and Umbria-Marche units).

The TMUs at the base of the nappe stack (Fig. 1a) experienced greenschist to blueschists facies metamorphism with carpholite-bearing assemblages reported in southern Tuscany (Di Pisa et al., 1985; Franceschelli et al., 1986; Theye et al., 1997; Giorgetti et al., 1998; Molli et al., 2000). Pressure peak conditions were reached around 24-18 Ma and were followed by a phase of exhumation in the middle Miocene (Kligfield et al., 1986; Brunet et al., 2000; Fellin et al., 2007). In Late Miocene times, the northern Apennines were characterized by a magmatic arc related to the development of the northern Tyrrhenian Sea as a back-arc basin (Boccaletti and Guazzone, 1972; Malinverno and Ryan, 1986), with intrusive and extrusive bodies mainly of crustal signature (Serri et al., 1993). In this framework, the Late Miocene magmatic products were interpreted as dating the onset of crustal extension. In addition, the progressive younging of magmatism from west to east supported a scenario of progressive eastward migration of the extensional front of the Apennines during the Miocene-Quaternary interval (Faccenna et al., 2001).

On the other hand, several seismic profiles image the hinterland of the Apennines as being significantly shortened by thrust faults with only poor evidence of extension (Ponziani et al., 1995; Cassano et al., 1998; Finetti et al., 2001). Further detailed structural investigations highlighted the existence of thrust faults controlling basement reactivation, growth of Miocene-Pliocene sedimentary basins (Boccaletti and Sani 1998; Bonini and Sani, 2002; Cerrina Feroni et al., 2006; Bonini et al., 2014) and emplacement of magmatic rocks (Musumeci et al., 2005, 2008). This has led some authors to infer the existence of a continuous or periodic compression in the northern Apennines until the Late Miocene or even Pliocene times (Boccaletti et al., 1999; Bonini and Sani, 2002; Musumeci et al., 2008; Bonini et al., 2014).

2.2 Geology of Elba Island

The structure of Elba Island is that of a large monocline formed by continental- and oceanic-derived nappes separated by north-south striking and west-dipping thrust faults (Barberi et al., 1967a; Pertusati et al., 1993; Keller and Coward, 1996; Massa et al., 2017). The nappe pile is subdivided into an Upper and a Lower Thrust complex, separated by a major thrust (Capo Norsi Thrust of Musumeci and Vaselli, 2012 or Rio Marina Thrust of Massa et al., 2017, in this work referred to as Capo Norsi Thrust, CNT), marked by tectonized serpentinites (Fig. 1b).

The Upper Thrust complex consists of units of oceanic affinity (Fig. 1b; Cretaceous Flysch, Paleogene Flysch and Ligurian Unit) overlying continent-derived units (Fig. 1b; Triassic – Oligocene Tuscan Nappe and Upper Carboniferous - Triassic Rio Marina Unit, the latter with lower greenschist facies metamorphism). The Lower Thrust complex (Fig. 1b) consists of the Ortano Unit, characterized by a Middle Ordovician basement (Musumeci et al., 2011) overlain by Jurassic – Oligocene cover, and the Calamita Unit, consisting of Lower Carboniferous basement (Musumeci et al., 2011) overlain by slices of Triassic – Jurassic rocks. The Lower Thrust complex is affected by greenschist to upper amphibolite facies metamorphism (Duranti et al. 1992; Mazzarini et al., 2011; Musumeci et al., 2011; Musumeci and Vaselli, 2012; Massa et al., 2016).

The west-dipping first-order architecture of Elba Island formed from a first Early Miocene, east-verging collisional stage (Keller and Coward, 1996; Pertusati et al., 1993; Massa et al., 2017), dated to about 19 Ma (Deino et al., 1992). The lowermost units (Calamita, Ortano and Rio Marina) were underthrusted and attained Early Miocene greenschist (Pandeli et al., 2001) to blueschist facies conditions (Bianco et al., 2015). During the Middle Miocene, the whole nappe stack, comprising the metamorphic unit exhumed at upper crustal levels, was in turn deformed by a Middle-Late Miocene out-of-sequence thrusting event (CNT; Fig. 1b), which led to tectonic repetition of the stack sequence and the development of a major east-verging fold in the Upper Thrust complex (Massa et al., 2017).

Nappe stacking was followed by the emplacement of Late Miocene magmatic bodies (Fig 1b), notably the Central Elba Sill Complex and the Monte Capanne Pluton in western Elba (8-7 Ma; Dini et al., 2002; Barboni and Shoene, 2014; Barboni et al., 2015) and the Porto Azzurro Pluton (Fig. 2; 5.9 – 6.7 Ma; Musumeci et al., 2015) in eastern Elba. The emplacement of large intrusives was responsible for the development of medium to high grade contact aureoles at pressures not exceeding 0.15-0.20 GPa (Duranti et al., 1992). The previous greenschist to blueschist metamorphic assemblages were strongly obliterated by low pressure contact metamorphism (Bouillin, 1983; Duranti et al., 1992; Rossetti et al., 2007). Similar low pressure (<0.2 GPa) contact metamorphism occurred also in mainland Tuscany, in the Larderello geothermal field (Fig. 1a), where still buried, large Pliocene-Pleistocene plutons caused contact aureoles ranging in thickness from 600 up to 1700 m (Musumeci et al., 2002; Bertini et al., 2006). Except Larderello and southeastern Elba, the northern Apennines metamorphic units are affected only by Early Miocene medium- to high-pressure metamorphism (e.g. Franceschelli et al., 1986; Giorgetti et al., 1998; Molli et al., 2000).

Decimetre to metre-scale folds and high- to low-angle fault zones documented in the contact aureoles have been classically related to either (i) pluton ballooning and gravitational collapse of the nappe stack (Pertusati et al., 1993; Westerman et al., 2004) or to the (ii) northern Tyrrhenian Sea opening-related crustal extension coeval with magma emplacement (Keller and Coward, 1996; Jolivet et al., 1998). However, in the contact aureole of the Porto Azzurro Pluton, Mazzarini et al. (2011) and Musumeci and Vaselli (2012) documented the occurrence of a kilometric N-S striking, open antiform of the regional foliation (Ripalte Antiform in Fig. 2) and of the Felciaio and Calanchiole shear zones (FSZ and CSZ in Fig. 2), two top-to-the-east decametre thick shear zones with thrust kinematics. The growth of the Ripalte Antiform controlled the site of emplacement of leucogranitic sheets and hydrothermal high temperature tourmaline veins (Mazzarini et al., 2011; Musumeci et al., 2015). The shear zones, characterized by the synkinematic growth of LP/HT mineral assemblages (Wo + Di + Tr + Tlc; abbreviations from Siivola and Schmidt, 2007), led to tectonic slicing of medium and high metamorphic grade rocks along the western side of contact aureole (Fig. 2; Musumeci and Vaselli, 2012).

3. The Calamita Unit

The Calamita Unit (Fig. 2) hosts the Porto Azzurro Pluton (Barberi et al., 1967b) and consists of:

- Calamita Schists, a monotonous sequence of metapelites, metarenites and quartzites (Barberi et al., 1967a,b) derived from Early Carboniferous flysch sequences (Musumeci et al., 2011);
- Barabarca quartzite, a thin slice of Middle Triassic metasandstones and metaconglomerates (Garfagnoli et al., 2005);
- Calanchiole marble, marbles and dolomitic marbles of Lower Jurassic age (Garfagnoli et al., 2005).

The contact between the Calanchiole marble and the underlying Calamita Schist and Barabarca quartzite is marked by the Calanchiole Shear Zone (Fig. 2; Musumeci and Vaselli, 2012).

The Porto Azzurro Pluton is a kilometre-scale buried intrusion, whose large size is suggested by the wide extent of its contact aureole (~60 km^2) throughout the Calamita Peninsula and eastern Elba Island (Musumeci and Vaselli, 2012). Moreover, gravimetric data in the northern Calamita Peninsula (Siniscalchi et al., 2008) and the finding of granitic rocks at 150–200 m in mining drill cores in eastern Elba (Bortolotti et al., 2001) also confirm that the roof of the intrusion is located at very shallow depths. The scattered exposures are formed by Bt-monzogranite apophyses, dated at 5.9±0.2 (^{40}Ar/^{39}Ar cooling age on Bt; Maineri et al. 2003), and a system of decimetre- to metre-thick leucogranite dykes (Eastern Elba Dyke Complex; Mazzarini and Musumeci 2008) dated at 6.3±0.2 Ma (^{40}Ar/^{39}Ar cooling age on magmatic muscovite; Musumeci et al., 2015). The differing cooling ages might result from multiple magmatic pulses or generations.

Contact metamorphism related to the pluton affects the Calamita Unit and part of the overlying Ortano Unit (Musumeci et al., 2015) leading to the development of a large-scale contact aureole. This aureole is largely exposed in the Calamita promontory and along the eastern coast of the Elba Island, and it is covered by the non-metamorphic rocks of the Upper Thrust Complex (Fig. 2).

The Calamita Schists and the Barabarca quartzite were equilibrated in the And + Crd + Bt + Ms zone (Musumeci and Vaselli, 2012), with the high grade metamorphic rocks (Bt + Crd + And + Kfs) occurring in the hinge zone of the Ripalte Antiform (Fig. 2; Mazzarini et al., 2011) along the eastern coast of the Calamita Promontory. A common feature in the metapelites is the occurrence of two generations of white mica. The earlier is associated with cordierite and aligned along the main foliation, whereas the later generation is grown static over the main foliation. In addition, andalusite, cordierite and K-feldspar are affected by widespread sericitization. The Calanchiole marble is characterized by medium to high metamorphic grade Cal + Dol + Phl + Di + Tr bearing paragenesis (Musumeci and Vaselli, 2012).

According to Duranti et al. (1992), the reported mineral assemblages suggest maximum pressures during contact metamorphism lower than 0.2 GPa and temperatures exceeding 650 °C. The age of contact metamorphism is constrained between 6.76±0.08 Ma and 6.33±0.07 Ma by means ^{40}Ar/^{39}Ar ages on phlogopite and biotite in the Calanchiole marble and Calamita Schists respectively (Musumeci et al., 2015). Furthermore, an U/Pb age on the rim of a detrital zircon yielded an age of 6.40±0.15 Ma (Musumeci et al., 2011), likely also dating contact metamorphism.

4. Deformation structures

Deformation structures in the Calamita Unit are represented by NNW-SSE striking metamorphic foliations, mesoscale folds and ductile to brittle fault zones. At the macro and mesoscopic scales the principal structural element of the Calamita Unit is the metamorphic foliation (Sp) folded around the open, N-NW trending upright Ripalte Antiform (Mazzarini et al., 2011; Figs. 2, 3). The western limb of the antiform is characterized by a gently to moderately west-dipping foliation and a main reverse shear zone (CSZ in Fig. 2; Musumeci and Vaselli, 2012). The CSZ is marked by mylonitic tremolite-bearing marbles and separates the Calanchiole marble in the hanging wall from the underlying Calamita Schists and Barabarca quartzite in the footwall (Fig. 2). A moderately to steeply east-dipping foliation occurs in the eastern fold limb.

At the mesoscale, in the Calamita Schists (Fig. 3) the Sp foliation is defined by the parallel arrangement of quartzite and metapelite-metapsammite layers and by the preferred orientation of mineral grains (And, Crd, Bt, Kfs and Wmca), defining a mineral lineation (Lp). At the microscale, the Sp is defined by alternating mica-rich domains and quartz-rich ribbons and/or lenses. The Sp represents the axial plane foliation of a system of east-verging non-cylindrical folds with axis orientation dispersed from N-S to E-W (Fig. 3g). Detailed field structural mapping outlined the existence of low- and high-strain domains heterogeneously distributed in the Calamita Schists (Figs. 3, 4). The low-strain domains represent the majority of the Calamita Schists, whereas the high-strain domains are metre- to decametre-thick zones of localized viscous deformation leading to proper mylonitic fabrics (Fig. 3).

At the meso-scale both low- and high-strain domains share the same orientation of Sp foliation and Lp lineation (Figs. 3, 4a). We use, therefore, the label SpL and LpL to describe the foliation and lineation in in low-strain domains and SpH and LpH in high-strain domains.

4.1 Low-strain domains

Low-strain domains (LSD) display a millimetre spaced SpL schistosity, corresponding to the axial plane foliation of metre to decimetre east-verging close to isoclinal asymmetric non-cylindrical folds with thickened hinges and variably thinned limbs (Fig. 4b). Foliation intensity increases along the reverse limb of folds. In the hinge zones of these folds, a previous foliation is preserved corresponding to recrystallized quartz-rich and mica-rich layers with partially preserved relic mineral assemblages consisting of quartz, white mica and opaque grains.

The SpL foliation is defined by the preferred orientation of Wmca + Bt + Qtz + And + Crd. Locally, millimetre- to centimetre-thick lenses containing randomly oriented radial aggregates of And + Crd + Bt are wrapped around by the foliation. The LpL lineation trends E to ENE, and plunges toward the west and the east, on the western and eastern limbs of the Ripalte Antiform respectively (Fig. 3). It is defined by quartz or aggregates of Bt, And and Crd. Leucogranite dykes emplaced in the low-strain domains are characterized by igneous fabrics (Mazzarini and Musumeci, 2008; Mazzarini et al., 2011).

4.2 High-strain domains

High-strain domains (HSD) are formed by NS-striking, centimetres- to metres- thick bands of intensely foliated And-Crd-bearing schist and quartzite (Fig. 3). At the map scale, they can be traced throughout the Calamita Unit and, due to the different extension of the limbs of the Ripalte Antiform, they are mainly exposed along the western limb of the antiform where they dip to the west (Figs. 3b, c, d). On the eastern limb of antiform, HSD dip to the east (Fig. 3e).

In the field, the transition from LSD to HSD is generally marked by a sharp lithological change from medium- to coarse-grained and weakly to moderately foliated schist to fine-grained and pervasively foliated schist with well developed SpH foliation. In metapelite, the foliation is defined by the tight alternation of strongly stretched quartz-rich layers and/or ribbons embedded in continuous biotite - white mica- rich andalusite-cordierite-bearing domains. In metapsammite, it corresponds to fine grained quartz - feldspar- rich layers with thin discontinuous mica- rich lenses (Figs. 4c, 5a). At the mesoscopic scale, SpH locally evolves into a mylonitic foliation mostly localized within the quartz-feldspathic lithologies (Fig. 5b).

The SpH bears clear lineations (LpH) formed by (i) elongated aggregates of Bt, Wmca and Qtz and (ii) oriented And, Crd, Kfs and Tur grains (Fig. 5c). As shown in Fig. 3, LpH has a constant EW to SW-NE direction in the entire Calamita Unit. It is also affected by the Ripalte Antiform, with West- and East-plunges in the western and eastern limbs, respectively. Field kinematic indicators, including S-C' fabrics (Fig. 5d), deflection of veins and dykes and asymmetric boudins, are consistent with an overall top-to-the-east sense of shear.

Boudinage of quartz layers and/or calcsilicate lenses embedded in the schist is also common, as highlighted by pinch-and-swell structures, symmetric boudins and asymmetric domino- or antithetic boudins. In the HSD, centimetre- to decimetre leucogranite dykes show foliated to mylonitic fabric parallel to the SpH foliation of the host rocks (Fig. 4a).

4.2.1 Calanchiole shear zone: a major high strain domain

The CSZ (Fig. 2) corresponds to a first order west-dipping high-strain zone characterized by a penetrative mylonitic foliation affecting both the footwall and hanging wall blocks (Fig. 3a). A cataclastic zone is found within the CSZ core (see par. 5.0). The CSZ dips generally to the west although locally it is characterized by flat segments (see par. 5.0). Its mylonitic marbles are characterized by the Cal + Dol + Di ± Phl and Cal + Dol + Tr ± Tlc mineral assemblage defining the W-dipping mylonitic foliation (Figs. 3a, 3d) that envelopes centimetre to decimetre thick boudins of andalusite- and cordierite-bearing metapelite. E-W trending LpH lineations in the CSZ are defined by elongated aggregates of Cal + Dol and grains of Tr, Tlc and Di and trend subparallel to LpH and LpL lineations in the footwall block (Fig. 3). East-verging, tight to isoclinal sheath folds (Fig. 5e) and mesoscopic duplexing of sheath folds (Fig. 5f), consistent with top-to-the-east shearing, are also common in the CSZ as described by Musumeci and Vaselli (2012) in the Calanchiole area. Moreover, at the base of the CSZ the mylonitic fabric is overprinted by brittle deformation with development of centimetre to decimetre thick foliated breccias and cataclasites (see section 5.0).

In the footwall of the CSZ (Fig. 3a), the Barabarca quartzite occurs as intensely deformed lenses below the Calanchiole marble. The quartzite exhibits a strong mylonitic schistosity (SpH) with aggregate lineations of Bt-Wmca and mineral lineations of And-Crd. Metaconglomerate lenses within the mylonitic quartzite show a strong linear fabric, defined by deformed quartz-tourmaline clasts, coherent with the mineral and stretching lineations in the Calanchiole marble and the Calamita Schists (Fig. 3).

4.3 Quartz microfabric

Over 100 samples (representative samples are listed in table S1) from low- and high-strain domains in the Calamita Unit have been collected and investigated in oriented thin section cut parallel to the Lp lineation and perpendicular to the Sp foliation (i.e. parallel to XZ plane of the finite strain ellipsoid), in order to study the relationships between meso-structures and microstructures with a specific focus on quartz-microfabric.

In the following sections we refer to microfabric as the complete spatial and geometrical configuration of all rock components at the microscale (sensu Passchier and Trouw, 2005).

Most of the samples described in the next sections have been collected in association with mesoscale structures (e.g. shear zones and meso-scale folds) well exposed in natural coastal sections in the western side of Calamita peninsula (Fig. S1).

4.3.1 Microfabric in low-strain domains

At the microscale, LSD are generally characterized by a foliated fabric marked by the aggregate shape preferred orientation of sub-parallel Wmca-Bt and Qtz-domains (Fig. 6a), defining the SpL. Andalusite and cordierite porphyroblasts occur as either contained within the SpL (Fig. 6b) or at high angle to it (Fig. 6c), resulting from a static overgrowth. Locally the SpL is partially overprinted by the static growth of also white mica crystals with coarse-grained, euhedral habits. In several samples, andalusite and K-feldspar are retrogressed to sericite and cordierite is masked by pinite alteration.

Quartz microfabric is characterized by subhedral to anhedral, inequant, medium to coarse-grained grains (100 μm up to 1-2 mm) showing amoeboid, interlobate to (rarely) polygonal grain boundaries (Fig. 6d). Reticular microstructures and island grains are common within low-strain domains. In layered domains separated by micas, the spacing of the mica domains generally controls quartz grain size, with coarser grains occurring in wide and pure quartz layers (e.g. Fig. 6d). Quartz in low-strain domains is weakly deformed as shown by undulose extinction and sparse recrystallized new grains of 10-100 µm in size that occur associated to small subgrains or bulging-microstructures.

4.3.2 Microfabric in high-strain domains

The SpH foliation in HSD at the microscale is defined by alternating mica-rich lepidoblastic domains and strongly elongated or stretched disequigranular coarse-grained to very fine-grained quartz- levels (Figs. 7a, b) that enclose stretched coarser-grained quartz grains (Fig.

7c). Mica-rich domains show a shape preferred orientation defined by subparallel white mica and biotite and contain synkinematic porphyroblasts of And and Crd (Fig. 7d). Kinematic indicators such as S-C' fabrics (Fig. 7e), sigma-type porphyroclasts mainly represented by asymmetric pinitized cordierite (Fig. 7f) and mica fish and are consistent with a top-to-the-east sense of shear.

Quartz-rich domains are arranged in millimetre (3-4 mm) to few hundreds (300-500 μm) microns thick ribbons and/or lenses often corresponding to the stretched limbs of isoclinal intrafoliar folds. In the mylonitic samples, quartz-rich domains are often crosscut by millimetres spaced C and C' shear planes defined by very-fine-grained quartz grains (see below).

4.4 Quartz microfabric in high-strain domains

Twenty representative samples with well developed quartz layers were selected for microfabric analysis. Based on grain size, grain shape and grain boundary type, three quartz microfabrics have been distinguished (Figs. 7a, b, c). We refer to them as stage 1, stage 2 and stage 3 microfabric implying their relative time sequence.

4.4.1 Stage 1 microfabric

Stage 1 microfabrics (Fig. 7a) are characterized by coarse-grained, irregularly shaped inequant (200 to 900 μm) to equant grains ranging between 400 to 600 μm in size. Quartz grain boundaries vary from amoeboid to interlobate (Figs. 8a, b). Locally, polygonal euhedral grains with straight boundaries also occur (Fig. 8c). Large quartz grains tend to form ~90° angles of intersection (reticular grains in Fig. 8b; Lister and Dornsiepen, 1982 and Jessel, 1987). Tiny grains (20-100 μm) in optical continuity with coarser-grained grains (island grains; Urai et al., 1986) occur close to grain boundaries or triple junctions (Fig. 8d). When associated to micas (i.e. Wmca or Bt), quartz is characterized by dragging, window, or pinning microstructures (Fig. 8e; Jessel, 1987).

Quartz grains show straight to sweeping undulose extinction and/or deformation bands. Some grains also show subgrain boundaries (size of subgrains: 10-100 μm; Fig. 8f) and are crossed by bands of stage 2 and 3 grains (Fig. 7c; see below). Quartz grains locally show a shape preferred orientation parallel to the SpH foliation (e.g. Fig. 8f). Aggregates of coarse quartz grains, extinct at the same time, indicate a lattice preferred orientation (Fig. 7a).

4.4.2 Stage 2 microfabric

Stage 2 microfabrics (Fig. 7b) consist of anhedral fine-grained (60 to 100 μm) equigranular and/or elongated grains with interlobate boundaries (Fig. 9a) characterized by straight to weak undulose extinction. As shown in Figs. 7b and 9a, a sharp decrease in grain size occurs between finer stage 2 grains and adjacent stage 1 grains. Stage 1 grains commonly contain subgrains comparable in shape and size to stage 2 grains (Figs. 9b, c).

Stage 2 grains commonly occur (i) along boundaries and triple junctions of stage 1 grains (Fig. 9b), (ii) as very fine aggregates of elongated grains (< 70 μm) in recrystallized ribbons and core-and-mantle structures wrapping relic stage 1 grains (Fig. 9c) and (ii) at the contact between quartz-rich and mica-rich domains. Strain caps around synkinematic andalusite and cordierite grains sometimes show local recrystallized stage 2 grains (Fig. 9d). In the limbs and hinge zones of microfolds (Fig. 9e) elongated stage 2 grains show a shape preferred orientation defining the SpH axial plane foliation (Fig. 9f).

4.4.3 Stage 3 microfabric

Stage 3 microfabric (Fig. 7c) is characterized by very fine-grained (less than 10 μm) quartz grains with anhedral shape and general straight extinction (Fig. 10a). In general, stage 3 grains occur as (i) bulges and limited aggregates at the grain boundaries between coarser stage 1 and 2 grains but in mylonitic samples (e.g. Fig. 7c) they form wide (ii) core-and-mantle structures and define (iii) conjugate sinistral and dextral shear bands cross-cutting relic coarse grains (Fig. 10b) and (iv) C'-shear bands. In both conjugate and C'-shear bands they display a moderate shape and lattice preferred orientation defining a foliation, oblique to the shear band and concordant with the sense of shear (Fig. 10c).

Stage 3 grains (Fig. 10d) are also associated to cataclastic bands in brittle fault zones (see section 5.1), where they strongly transpose relic stage 1 and stage 2 grains (Fig. 10a) cross-cut by conjugate sets of healed fractures or shear bands, marked by non-oriented stage 3 grains (Fig. 10d).

5. Brittle deformation structures

5.1 Brittle fault zones

The Calamita Schists are locally characterized by the occurrence of centimetric to decimetric low-angle east-dipping brittle fault zones. The best examples crop out in sector C (Fig. 3c). Here, east dipping (5-15°) decimetric fault zones (Y-shears; Figs. 11a, b) cut across the west-dipping (40-50°; Fig. 3c) SpH foliation in the Calamita Schists (Fig. 11c). Y-shears consist of unfoliated cohesive cataclasite associated with centimetric foliated ultracataclasite bands that are generally localized at the uppermost portion of the Y-shear fault zones (Fig. 11c). Slip planes are decorated with quartz fibres defining E-W trending slickenlines (Fig. 3h). Based on the position of markers in the footwall and hanging wall blocks, the total displacement measured along these Y-shears ranges between 10 and 20 metres. Y-shears are associated with (i) moderately dipping (20-30°; Fig, 11b) synthetic top-to-the-east fault planes (R-shears; Fig. 11a) and (ii) antithetic top-to-the-west steeply east-dipping (60-70°) fault planes (R'-shears; Fig. 11a, b). R- and R'-shears mutually intersect, sometimes displacing also Y-shears

(Fig. 11a). Wedge shaped cataclasite layers Fig. 11a) bounded by R- and R'-shears are common. Other brittle fault zones marked by R-, R'- and Y-shears, occur sparsely in the Calamita Schists in areas of high fractures density, sometimes displacing leucogranite dykes (Figs. 3b, d).

At the microscale, Y-shears show an abrupt passage from mylonite in the walls to cataclasite in the fault core zone with a centimetric ultracataclasite located at the contact with the hanging wall block (Fig. 11d). The ultracataclasite layers consist of millimetric quartzite and schist clasts embedded in a very fine-grained matrix (< 5 μm) made of quartz and mica (Fig. 11d). At the contact with the fault zones, wall rocks are characterized by shear fractures parallel to the fault surface (Fig. 11d).

6. Discussion

6.1 Deformation in the Calamita Unit: geometries and fabrics

In the Calamita Unit deformation structures coeval with contact metamorphism were first recognized by Debenedetti (1953), who described the occurrence of mylonitic-cataclastic layers. Later, Pertusati et al. (1993) interpreted the dominant foliation in the Ortano Unit as evidence of local deformation related to magma emplacement. More recently, Mazzarini et al. (2011) and Musumeci and Vaselli (2012) provided evidence of large-scale deformation in the south-eastern Elba Island coeval with pluton emplacement.

On the basis of the field and microstructural data presented here, the dominant features of the Calamita Unit can be summarized as follows:

(i) occurrence of low- and high-strain domains, (ii) W-dipping shear zones with overall top-to-the-east shear sense, (iii) non cylindrical to sheath-like east-verging folds; (iv) E-W trending mineral lineations, and (v) synkinematic growth of HT/LP mineral assemblages in high-strain domains. These data highlight that the main fabric of the Calamita Unit (Sp) is characterized by: (i) late Miocene medium- to high-grade metamorphism related to the thermal anomaly due to emplacement of igneous bodies at shallow crustal level ($P \leq 0.2$ GPa) and (ii) deformation partitioning in low- and high-strain domains. The reconstructed tectonic setting of the Calamita Unit is shown in Fig. 3. The main high-strain domain corresponds to the east-verging Calanchiole shear zone (CSZ) that occurs in the western side of the Calamita Unit and is associated with diopside-bearing to tremolite- talc-bearing mylonitic marble, which indicates the contemporaneity between deformation and thermal anomaly (Musumeci and Vaselli, 2012). In the underlying Calamita Schists, high-strain domains, parallel to the CSZ, show a heterogeneous distribution (see Fig. 3) with an along-strike continuity ranging from the hectometre to some kilometres. E-W trending lineations and kinematic indicators (Fig. 3) support an overall east-verging direction of tectonic transport. The general attitude of foliations and lineations (see Fig. 3) reveals neither deviations nor relevant rotations of structural elements throughout the whole Calamita Unit along both N-S and E-W directions. Moreover, the parallelism of the Sp foliation in both low and high-strain domains and its opposite dip on the western and eastern limbs of the Ripalte Antiform, indicate that the foliated fabric, shear zones, and lineations were folded by the Ripalte Antiform during a late stage. The documented, later brittle overprint is expressed by (i) brittle fault zones reworking all previous fabrics (SpL and SpH) and (ii) first and second order Riedel systems and (iii) E-W directed slickenlines associated with top-to-the-east shear sense indicators.

6.2 Quartz microstructures: insight onto a deformation history in high strain domains

Quartz microstructures are commonly used to semi quantitatively constrain deformation temperature, kinematics and deformation regime in collisional belts (Srivastava and Mitra, 1996; Faghih & Sarkarinejad, 2011; Law, 2014; Frassi, 2015) and pluton aureoles (e.g. Stipp et al., 2002b and Morgan and Law, 2004). Several factors influence and steer the active mechanisms of quartz deformation, such as temperature (Stipp et al., 2002a, b), differential stress, strain rate (e.g. Pennacchioni et al., 2010; Kidder et al., 2016) and the presence of water in the crystal lattice or at the grain boundaries (Selverstone, 2005; Menegon et al., 2011; Kilian et al., 2016; Morgan et al., 2016). Except these parameters, according to Stipp et al. (2002a; 2010), the mechanisms of dynamic recrystallization of quartz vary primarily as a function of temperature during deformation. Two are the competing processes during quartz recrystallization: (i) the migration of existing grain boundaries (grain boundary migration; Poirier and Guillopè, 1979; Means, 1983; Poirier, 1985; Drury and Humpreys, 1986) and (ii) the formation of new grain boundaries after rotation of the crystal lattice of a subgrain boundary (subgrain rotation; Poirier and Nicolas, 1975; White, 1977; Guillopé and Poirier, 1979). Subgrain rotation and grain boundary migration do not operate independently during deformation of natural rocks (Stipp et al., 2002a) and their mutual interaction occurs in several ways depending on the temperature of deformation. In particular there are three main deformation mechanisms active for quartz, which, for increasing temperature, are (Stipp et al., 2010): (i) bulging (BLG), (ii) subgrain rotation (SGR) and (iii) grain boundary migration (GBM) recrystallization.

Stage 1 microfabrics in high-strain domains (Fig. 8) are characterized by several microstructures indicating the fast movement of grain boundaries like island grains (Fig. 8d) or pinning microstructures (Fig. 8e), fitting well the features typical of GBM-recrystallization mechanisms. In addition the occurrence of i) quartz grains clearly overgrowing subparallel micas defining the foliation (Fig. 8e) and ii) large areas where quartz grains share the same crystallographic orientation (Fig. 7a) indicate that crystal plasticity occurred along with GBM. Morgan et al. (2016) reported similar microstructures in the most strained areas of the contact aureole surrounding the Eureka-Joshua Flat-Beer Creek pluton.

Stage 2 microfabrics (Fig. 9) overprint relic stage 1 grains forming aggregates along grain boundaries (Fig. 9b), core-and-mantle structures and ribbons of elongate grains (Figs. 7b, 9c). In particular, relic stage 1 grains display subgrains with the same size and shape of stage 2 grains (Figs. 9b, c). These microstructures have been classically interpreted as evidence for SGR-recrystallization (e.g. Stipp et al., 2002) and indicate that stage 2 grains formed after the rotation of subgrains embedded in relic stage 1 grains.

Stage 3 microfabrics (Figs. 7c, 10) overprint both stage 1 and 2 grains along grain boundaries forming bulges and tiny aggregates that can be interpreted as resulting from dominant BLG-recrystallization, as described by Stipp et al. (2002). Furthermore, stage 3 grains occur closely associated to shear bands and cataclasites forming trails of tiny grains. Similar microstructures have indeed been described in quartz-bearing lithotypes deformed at low-grade metamorphic conditions e.g. by Kjøll et al., (2015) and interpreted as a result of low-temperature processes such as pressure-solution creep or low-temperature plasticity (e.g. Trepmann et al., 2017).

Moreover, the average quartz grain size of the three described microfabrics (stage 1, 2 and 3) is consistent with the recrystallized quartz grain size distribution provided in the review of Stipp et al. (2010). Indeed, stage 1 microfabric grains, characterized by 200-800 µm grain size, fit well the grain size range for GBM in the data set of Stipp et al. (2010). Also, stage 2 (60-100 µm) and stage 3 grains (<10 µm) are comparable in size to SGR- and BLG-grains in the data set of Stipp et al. (2010).

The sketch in Fig. 12 illustrates the relationships between GBM-, SGR- and BLG-recrystallization recorded by quartz microfabric. GBM-dominated fabrics occur in strict association with the peak metamorphic assemblage that has been constrained by Duranti et al. (1992) at >650 °C. This temperature is consistent with the data of Stipp et al. (2002a, b) that constrained the GBM-zone of the Adamello pluton above 500 °C. Along the same SpH foliation, the GBM-fabric is then progressively overprinted by SGR-dominated recrystallization, forming elongate ribbons of new grains around relics of grains with GBM-microstructures, and BLG-recrystallization, the latter associated with shear fractures and incipient brittle deformation (Fig. 12). Similar bands of recrystallized BLG-new grains in large porphyroclasts have been described in several studies and interpreted as evidence of low-grade deformation (Kjøll et al., 2015). In addition, the ductile quartz fabric is overprinted by cataclasis, indicating that deformation continued in the brittle regime, at least below the classically reported temperatures for the brittle-ductile transition of quartz (~300 °C; e.g. Voll, 1976; 250±20 °C; Dunlap et al., 1997).

In particular, (i) the strict association between GBM-microstructures and the metamorphic peak assemblage (i.e. And + Crd + Kfs) and (ii) the cataclastic overprint over the ductile fabric, suggest that temperature was the main controlling parameter during deformation in the high-strain zones of the Calamita Unit. The diminishing temperature is likely associated with the vanishing thermal pulse related to the cooling Porto Azzurro Pluton, as already demonstrated by Musumeci and Vaselli (2012) and Musumeci et al. (2015). Cataclastic structures can be interpreted as the restoration of the brittle deformation regime after the end of the thermal pulse, that is consistent with the upper crustal setting of Calamita Unit (< 0.2 GPa) assuming a geothermal gradient of 25°C km^{-1}.

6.3 Age of deformation

Among the available radiometric ages for the Calamita Unit, the 6.76±0.08 Ma $^{40}Ar/^{39}Ar$ Phl age on Di-Phl marble and 6.23±0.06 Ma $^{40}Ar/^{39}Ar$ age on late Ms in And-Crd-Bt schists

(Musumeci et al., 2011, 2015) provide lower and upper limits for ductile deformation. This age interval is corroborated by the 6.40±0.15 Ma U/Pb age on zircon (Musumeci et al., 2011). Interestingly, available age constraints are younger for the magmatic rocks emplaced in the Calamita Unit. A mylonitic leucogranitic dyke injected in a high-strain domain yielded a $^{40}Ar/^{39}Ar$ Ms age of 6.33±0.07 Ma (Musumeci et al., 2015) and the exposed monzogranite yielded a cooling age of 5.9±0.2 Ma ($^{40}Ar/^{39}Ar$ on Bt; Maineri et al., 2003). Thus, the leucogranitic dykes and monzogranite body, commonly referred to as the exposed part of the Porto Azzurro Pluton, *de facto* postdate the thermal peak. This is also suggested by the evolved compositions of these magmatic products (Peretti, 2007) and supports the hypothesis of Marinelli (1959) that the areal extent of the aureole should be related to a buried pluton, less evolved than the acid exposed igneous rocks. Furthermore, from a structural point of view, this is consistent with the cross-cutting relationships between the Dyke Complex (Mazzarini and Musumeci, 2008), the monzogranite and their surrounding host rocks. The age of the mylonitic dykes (6.3 Ma) overlaps with the Ms-age in the host metamorphic rocks and might be regarded as the lower limit for transition from ductile to brittle deformation. A reasonable upper limit for semi-brittle deformation in the aureole is provided by the relative age of the brittle Zuccale Fault, which crosscuts all the structures and magmatic rocks within the Calamita Unit. According to Musumeci et al. (2015), the activity of Zuccale is bracketed between 6.23±0.06 Ma ($^{40}Ar/^{39}Ar$ on Ms; youngest available age of footwall rocks) and 5.39±0.46 Ma (U-Th-He on adularia-specularite mineralization in the hanging wall; Lippolt et al., 1995).

7. Tectonic vs. pluton deformation

The described meso and microstructural features in the Calamita Unit and the available radiometric data provide clear evidence of a long lasting deformation (300-500 kyr) within an overall top-to-the east kinematic framework within which early ductile structures were overprinted by later brittle structures.

In order to discriminate between regional scale- and magma emplacement-related deformation, the following points should be considered (see Fig. 13):

1) constant N to NNE strike of foliation and trend of fold axes, as well as E-W trending mineral/slickenside lineations;
2) nearly constant eastward sense of tectonic transport that characterizes both ductile and brittle structures;
3) abrupt strain gradient defined by the occurrence of high-strain zones distributed throughout the Calamita Unit and their parallelism with the main Calanchiole and Felciaio Shear Zones (Musumeci and Vaselli, 2012). The former is the main ductile-brittle structure well away from the inferred contact with the intrusive body (see Fig. 2 and cross sections in Fig. 13), the latter in the outer portion of the contact aureole (Ortano Unit) led to tectonic doubling of the aureole (Musumeci and Vaselli, 2012);
4) upright geometry of the Ripalte Antiform as well as that of mesoscopic scale folds that refold SpL and SpH ductile fabrics in both low- and high- strain domains;
5) geometrical location of all deformation structures above the roof of the intrusion and their attitude, which is consistent with subhorizontal shortening instead of vertical flattening. In addition, in the case of deformation structures related to a pluton inflating upward, the shear sense would be opposite on both sides of the antiform (i.e. top-to-the west on the western limb of the antiform). This is not the case for the described example, where the geometry of the structural elements in the aureole is independent from that of the buried Porto Azzurro Pluton.

A possible interpretation of the Calamita Unit is shown in Fig. 13.Based on the (i) presented data and (ii) large-scale structural setting of the central-eastern Elba Island (Mazzarini et al., 2011; Musumeci and Vaselli 2012; Musumeci et al. 2015), we interpret the Calamita Unit as bound by two main thrust zones. The upper structure corresponds to the Capo Norsi Thrust at the base of the Upper Thrust Complex, which discordantly superimposes non-metamorphic rocks onto high metamorphic grade hornfels rocks belonging to the Calamita and Ortano Units (Musumeci and Vaselli, 2012). This means that although this thrust was possibly active during the Early to Middle Miocene nappe stacking (Keller and Coward, 1996; Massa et al., 2017), its last phase of activity outlasted the final stage of thermal anomaly in the underlying Lower Thrust Complex. The lower thrust structure is not exposed, but its occurrence can be inferred from the presence of the Ripalte Antiform (Mazzarini et al., 2011), whose reconstructed geometry can be related to that of a thrust-related fold developed on a ramp segment. As shown in the cross sections in Fig. 13, the igneous intrusion underlies the whole antiform from the western to the eastern limb. Both host rocks and igneous intrusion rest on the hanging wall of the inferred thrust (Fig. 13). According to this reconstruction, the upper and lower thrusts are the roof and floor thrusts of a large scale duplex structure, where the high-strain domains coincide with and represent the duplexes high-strain bounding zones.

The documented features support a model wherein the structures in the Calamita Unit resulted from the interaction between large-scale tectonics and a magma emplacement-related transient and localized thermal anomaly. Similar deformative structures have been documented worldwide in aureoles related to plutons emplaced in several orogenic belts, but very few examples of deformation in upper crustal aureoles are documented so far.

The contact aureole of the Eureka-Joshua Flat-Beer Creek pluton (Morgan et al., 2016) is an example of shallow crustal level pluton (P ~ 0.3 GPa), whose emplacement led to host rock deformation concentrated in the inner aureole, where metasedimentary wall rocks were significantly shortened (60 - 70%) all around the composite pluton. Furthermore, in the southern side of the pluton the regional foliation shows a significant change of strike from NS to WNW in the deformed inner aureole. Rotation of the regional foliation was accompanied by a change in the dip angle from moderate to steep, with the development of a new cleavage parallel to the contact between the pluton and the aureole.

The Adamello Pluton, emplaced close to the Tonale Fault in the central Alps (Schimd et al., 1996), is another example of contact metamorphism and coeval shearing along a regional fault zone at shallow crustal levels (0.25 - 0.35 GPa; Stipp et al., 2002a; John and Blundy, 1993). As stated by Stipp et al. (2004), although the Adamello Pluton and the Tonale Fault are not genetically linked, strike-slip deformation interacted with the contact aureole giving rise to a mylonitic belt made up of variably deformed contact metamorphic schist. Within this belt, the metamorphic grade increases southward in direction of the pluton and the shear strain increases northward in the direction of the Tonale Fault zone.

These two examples represent end-members of interaction between tectonics and magmatism. In the former case, structures in the contact aureole of Eureka-Joshua Flat- Beer Creek pluton have been interpreted as evidence of an expanding pluton with magma emplacement-related deformation leading to outward translation of wall rocks and stretching of the inner aureole (Morgan et al., 2013). In the latter case, the contact aureole of the Adamello Pluton represents an aureole where the distribution of tectonic structures is independent from the geometry of the intrusive body and is instead steered by the regional background deformation (Stipp et al 2004).

Our new data support the interpretation that the Calamita Unit is a contact aureole formed during ongoing regional scale E-W compressive deformation, with high-strain zones and a large foliation dome (see Fig. 13). The effects of the underlying pluton on the aureole geometry appear to have been minimal. Tectonically-assisted emplacement of intrusions within fault-bend folds in fold-and-thrust belts was reported, for example, in the Sevier orogenic belt (Kalakay et al., 2001) and in the mainland Northern Apennines (e.g. in the Gavorrano area; Musumeci et al., 2005; Fig. 1). Among the many documented synkinematic plutons (e.g. Collins and Sawyer, 1996; Benn et al., 1998; Stipp et al., 2004; Nabelek and Morgan, 2012), this is however one of the few showing thrust-related deformation of a synkinematic buried intrusion, as revealed by deformation patterns in the contact aureole.

8. Conclusions

Based on new structural and microstructural data, we document an example of shallow crustal level contact aureole, where localized domains of deformation resulted from the interplay between regional scale deformation and localized transient thermal anomaly related to the emplacement of Late Miocene igneous rocks.

Deformation was characterized by the heterogeneous distribution of low- and high-strain domains, documentable at all scales. High-strain domains consist of strongly foliated rocks with localized mylonitic bands showing top-to-the-east sense of shear. In these domains, quartz recorded a retrogressive evolution from high temperature to low temperature conditions. Top-to-the-east cataclastic deformation invariably overprints earlier ductile fabrics and provides evidence that deformation outlasted the effects of the thermal anomaly and continued through to very low temperature conditions (T< 300 °C). The tectonic evolution of the Calamita Unit contact aureole highlights that, in the northern Tyrrhenian Sea area, Late Miocene regional-scale collisional tectonics controlled upper crustal deformation and the site of magma emplacement.

Aknowledgements

The authors wish to thank Chiara Frassi for her helpful comments on an earlier version of this manuscript and Giulio Viola for his comments and accurate reading of the manuscript. The constructive reviews by Sven Morgan and Elena Druguet, and the meticulous editorial work of Philippe Agard were very helpful in improving the original manuscript and are gratefully acknowledged. This project has been funded by PRA_2016 (Resp. Sergio Rocchi) of the University of Pisa.

References

Bailey, J.E., Hirsch, P.B., 1962. The recrystallization process in some polycrystalline metals. Proceedings of the Royal Society of London A 267, 11-30.

Bally, A.W., L., Burbi, C., Cooper, R., Ghelardoni, 1986. Balanced sections and seismic reflection profiles across the central Apennines. Memorie della Società Geologica Italiana 35, 257–310.

Barberi, F., Giglia, G., Innocenti, F., Marinelli, G., Raggi, G., Ricci, C.A., Squarci, P., Taffi, L., Trevisan L., 1967a. Carta geologica dell'isola d'Elba scala 1:25.000. C.N.R. Roma.

Barberi, F., Innocenti F., Ricci, C.A., 1967b. Il complesso scistoso di Capo Calamita (Isola d'Elba). Atti Soc. Toscana Sci. Nat. Pisa, Mem., P.V., Ser. A, 72 (2), 579-617.

Barboni, M., Schoene B., 2014.Short eruption window revealed by absolute crystal growth rates in a granitic magma. Nat. Geosci. 7, 524–528.

Barboni, M., Annen, C., Schoene, B., 2015. Evaluating the construction and evolution of upper crustal magma reservoirs with coupled U/Pb zircon geochronology and thermal modeling: A case study from the Mt. Capanne pluton (Elba, Italy). Earth Pl. Sci. Lett. 432, 436-448.

Benn, K., Ham, N.M., Pignotta, G.S., 1998. Emplacement and deformation of granites during transpression: magmatic fabric of the Achaean Sparrow pluton, Slave Province, Canada. Journal of Structural Geology, 20, 1247-1259.

Bertini, G., Casini, G., Gianelli, G. Pandeli, E. 2006. Geological structure of the Larderello

geothermal field.Terra Nova, 18, 163–169.
Bianco, C., Brogi, A., Caggianelli, A., Giorgetti, G., Liotta, D., Meccheri, M., 2015. HP-LT metamorphism in Elba Island: Implications for the geodynamic evolution of the inner Northern Apennines (Italy). J. Geod., 91, doi: 10.1016/j.jog.2015.08.001
Blumenfeld, P., Mainprice, D., Bouchez, J.L., 1986. C-slip in quartz from subsolidus deformed granite. Tectonophysics 127, 97-115.
Boccaletti, M., Guazzone, G., 1972. Gli archi appenninici, il Mar Ligure ed il Tirreno nel quadro della tettonica dei bacini marginali di retro-arco. Mem. Soc. Geol. It., 11, 201-216.
Boccaletti, M., Elter, P. Guazzone, G., 1971. Plate tectonics model for the development of the western Alps and northern Apennines. Nature, 234, 108–111.
Boccaletti, M., Bonini, M., Moratti, G., Sani, F., 1999.Compressive Neogene-Quaternary tectonics in the hinterland area of the Northern Apennines, In: Boccaletti, M., M. Dahmani nd G. Moratti (Eds.), Neogene Sedimentation and Tectonics in the Western Mediterranean. J. Petr. Geol., 22, pp-37-60.
Bonini, M., Sani, F., 2002. Extension and compression in the Northern Apennines (Italy) hinterland: evidence from the Late Miocene-Pliocene Siena-Radicofani Basin and relations with basement structures. Tectonics 21, 1010, doi: 10.1029/2001TC900024
Bonini, M., Sani, F., Stucchi, E.M., Moratti, G., Benvenuti, M., Menanno, G., Tanini, C., 2014. Late Miocene shortening of the Northern Apennines back-arc. J. Geodyn. 74, 1-31, doi: 10.1016/j.jog.2013.11.002.
Bortolotti, V., Fazzuoli, M., Pandeli, E., Principi, G., Babbini, A., Corti, S., 2001. Geology of Central and Eastern Elba Island, Italy. Ofioliti 26 (2a), 97-150.
Bouillin, J.P., 1983. Exemples de deformation locale liées à la mis en place de granitoides alpins dans des conditions distensives: l’ile d’Elbe (Italie) et le Cap Bougaron (Algérie). Rev. Geol. Dyn. Geogr. Phys., 24, 101–116.

Brunet, C., Monié, P., Jolivet, L., Cadet, J.P., 2000. Migration of compression and extension in the Tyrrhenian Sea, insights from 40Ar/39Ar ages on micas along a transect from Corsica to Tuscany. Tectonophysics 321, 127–155.

Cassano, E., Anelli, L., Cappelli, V, La Torre, P., 1998. Interpretation of Northern-Apennine magnetic and gravity data in relation to the profile Crop-03.Memorie della Società Geologica Italiana 52, 413–425.

Cerrina Feroni, A., Bonini, M., Martinelli, P., Moratti, G., Sani, F., Montanari, D., Del Ventisette, C., 2006. Lithological control on thrust-related deformation in the Sassa-Guardistallo Basin (Northern Apennines hinterland, Italy). Basin Research 18, 301–321.

Collettini, C., Holdsworth, R. E., 2004. Fault zone weakening and character of slip along low-angle normal faults: Insights from the Zuccale Fault, Elba, Italy. J. Geol. Soc., 161, 1039–1051.

Collins, W.J., Sawyer E.W., 1996. Pervasive granitoid magma transfer through the lower-middle crust during non-coaxial compressional deformation. Journal Metamorphic Geology, 14, 565-579.

Cruden, A.R., Mazzarini, F., Bunger, A.P., Musumeci, G., 2009.Geometry, scaling relationships, and emplacement dynamics of ca. 6 Ma shallow felsic sill complex, Calamita Peninsula, Elba Island, Italy. EOS Trans. AGU, 90, Abstract T13A-1843.

Deino, A., Keller, J.V.A., Minelli, G., Pialli G., 1992. Datazioni 40Ar/39Ar del metamorfismo dell'Unità di Ortano-Rio Marina (Isola d'Elba): Risultati preliminari. Stud. Geol. Camerti, 2, 187–192.

Di Pisa, A., Franceschelli, M., Leoni, L., Meccheri, M., 1985. Regional variation of the metamorphic temperature across the Tuscanid I Unit and its implication on the alpine metamorphism (Apuan Alps, N Tuscany).Neues Jahrbuch fur Mineralogie-Abhandlungen 151, 197-211.

Dini, A., Musumeci, G., Mazzarini, F., Rocchi, S., 2008. Multiple hydro-fracturing by boron-rich fluids in the Late Miocene contact aureole of eastern Elba Island (Tuscany, Italy). Terra Nova 20, 318-326.

Dini, A., Innocenti, F., Rocchi, S., Tonarini, S., Westerman, D.S., 2002. The magmatic evolution of the late Miocene laccolith–pluton–dyke granitic complex of Elba Island, Italy. Geol. Mag., 139, 257–279.

Drury, M.R., Humphreys, F.J., 1986. The development of microstructure in Al-5% Mg during high temperature deformation. Acta Metallurgica 34, 2259-2271.

Drury, M.R., Humphreys, F.J., White, S.H., 1985. Large strain deformation studies using polycrystalline magnesium as a rock analogue. Part II: dynamic recrystallization mechanisms at high temperatures. Physics of the Earth and Planetary Interiors 40, 208-222.

Dunlap, W.J., Hirth, G., Teyssier, C., 1997. Thermomechanical evolution of a ductile duplex. Tectonics 16, 983-1000.

Duranti, S., Palmeri, R., Pertusati, P.C., Ricci C.A., 1992. Geological evolution and metamorphic petrology of the basal sequence of eastern Elba (complex II).Acta Vulcanologica, 2, 213–229.

Elter, P., 1975. Introduction a` la géologie de l'Apennin septentrional. Bull. Soc. Geol. Fr., 7, 956–962.

Faccenna, C., Funiciello, F., Giardini D., Lucente P., 2001. Episodic back-arc extension during restricted mantle convection in the central Mediterranean. Earth Plan. Sci. Lett., 187, 105-116.

Faghih, A., Sarkarinejad, K., 2011. Kinematics of rock flow and fabric development associated with shear deformation within the Zagros transpression zone, Iran. Geol. Mag. 148, 1009-1017.

Franceschelli, M., Leoni, L., Memmi, I. and Puxeddu, M., 1986. Regional distribution of

Al-silicates and metamorphic zonation in the low-grade Verrucano metasediments from the Northern Apennines, Italy. Journal of Metamorphic Geology, 4(3), 309-321.

Frassi C. 2015. Kinematic constrains and deformation temperature from the lower portion of the Greater Himalayan Sequence in the Chaudabise river valley (West Nepal). Journal of Structural Geology, 81, 28-44.

Fellin, M.G., Reiners, P.W., Brandon, M.T., Wüthrich, E., Balestrieri, M.L., Molli, G., 2007. Thermochronologic evidence for the exhumational history of the Alpi Apuane metamorphic core complex, northern Apennines, Italy. Tectonics 26, doi: http://dx.doi.org/10.1029/2006TC002085.

Finetti, I.R., Boccaletti, M., Bonini, M., Del Ben, A., Geletti, R., Pipan, M., Sani, F., 2001. Crustal section based on CROP seismic data across the North Tyrrhenian-Northern Apennines-Adriatic Sea. Tectonophysics 343, 135–163.

Franceschelli, M., Leoni, L., Memmi, I., Puxeddu M., 1986.Regional distribution of Al-silicates and metamorphic zonation in the low-grade Verrucano metasediments from the Northern Apennines.J. of Metamorphic Geology 4, 309-321.

Garfagnoli, F., Menna, F., Pandeli, E., Principi, G., 2005. The Porto Azzurro Unit (Mt. Calamita promontory, south eastern Elba Island, Tuscany): stratigraphic, tectonic and metamorphic evolution. Boll. Soc. Geo. Ita., Volume Speciale 3, 119-138.

Giorgetti, G., Goffé, B., Memmi, I., Nieto, F., 1998. Metamorphic evolution of Verrucano metasediments in Northern Apennines: new petrological constraints. European Journal of Mineralogy 10, 1295-1308.

Guillopé, M., Poirier, J.P., 1979. Dynamic recrystallization during creep of single-crystalline halite: an experimental study. Journal of Geophysical Research 84, 5557-5567.

Hannula, K.A., Lackey, J.S., Mattox, E., McGrath. G., Onasch, E., Wertheim. J., 1999. Syn-tectonic pluton intrusion during contractional deformation: microstructural and metamorphic evidence from the aureole of the Acadian Victoria Pluton, north-eastern Vermont, USA. Journal of Metamorphic geology 17, 271-286.

Hirth, G., Tullis, J., 1992. Dislocation creep regimes in quartz aggregates. Journal of Structural Geology 14, 145-159.

Hutton, D.H.W., 1988. Granite emplacement mechanism and tectonic controls: inferences from deformation studies. Transaction of the Royal Society of Edinburgh: Earth Science, 79, 245-255.

Jessel, M.W., 1987. Grain-boundary migration mesostructures in a naturally deformed quartzite. Journal of Structural Geology 9, 1007-1014.

John, B.E., Blundy, J.D., 1993. Emplacement-related deformation of granitoid magmas, southern Adamello Massif, Italy.Geological Society of American Bulletin 105, 12, 1517-1541, doi: 10.1130/0016-7606.

Jolivet, L., Faccenna, C., Goffé, B., Mattei, M., Rossetti, F., Brunet, C., Storti, F., Funiciello, R., Cadet, J.P., D’Agostino, N., Parra, T., 1998. Midcrustal shear zones in postorogenic extension: Example from the northern Thyrrenian Sea. J. Geophys. Res. 103, 12123-12160.

Kalakay, T.J., John, B.E., Lagerson, D.R., 2001. Fault-controlled pluton emplacement in the Sevier fold-and-thrust belt of southwest Montana, USA. Journal of Structural Geology 23, 1151-1165.

Karlstrom, K.E., Williams, M.L., 1995. The case of simultaneous deformation, metamorphism and plutonism: an example from Proterozoic rocks in central Arizona. Journal of Structural geology, 17, 1, 59-81.

Keller, J.V.A., Coward, M.P., 1996. The structure and evolution of the northern Tyrrhenian Sea. Geol. Mag., 103, 1–16.

Kidder, S., Hirth, G., Avouac, J.P. and Behr, W., 2016.The influence of stress history on the grain size and microstructure of experimentally deformed quartzite. Journal of Structural Geology, 83, 194-206.

Kilian, R., Heilbronner, R., Holyoke, C.W., Kronenberg, A.K. and Stünitz, H., 2016. Dislocation creep of dry quartz. Journal of Geophysical Research: Solid Earth, 121(5), 3278-3299.

Kjøll, H.J., Viola, G., Menegon, L., Sorensen, B.E., 2015. Brittle-viscous deformation of vein quartz under fluid-rich lower greenschist facies conditions.Solid Earth 6, 681-699.

Kligfield, R., Hunziker, J., Dallmeyer, R.D., Schamel, S., 1986. Dating of deformational phases using K-Ar and ^{40}Ar/^{39}Ar techniques: results from the Northern Apennines. J. Struct. Geol., 8, 781–798.

Law, R.D., 2014. Deformation thermometry based on quartz c-axis fabrics and recrystallization microstructures: A review. Journal of Structural Geology, 66, 129-161.

Lippolt, H.J., Wernicke, R.S., Bahr., R., 1995. Paragenetic specularite and adularia (Elba, Italy): Concordant (U + Th)–He and K-Ar ages. Earth Planet. Sci. Lett., 132, 43–51.

Lister, G.S., Dornsiepen, U.F., 1982. Fabric transitions in the Saxony granulite terrain. Journal of Structural Geology 4, 81-92.

Lloyd, G.E., Freeman, B., 1994. Dynamic recrystallization of quartz and quartzites.Journal of Structural Geology 16, 867-881.

Mainprice, D., Bouchez, J.L., Blumenfeld, P., Tubia, J.M., 1986. Dominant c-slip in naturally deformed quartz: implications for dramatic plastic softening at high temperature. Geology 14, 819-822.

Maineri, C., Benvenuti, M., Costagliola, P., Dini, A., Lattanzi, P., Ruggieri, C., Villa., I.M., 2003. Sericitic alteration at the La Crocetta mine (Elba Island, Italy): Interplay between magmatism, tectonics, and hydrothermal activity. Miner. Deposita, 38, 67–86.

Malinverno, A., Ryan, W.B.F., 1986. Extension in Tyrrhenian Sea and shortening in the

Apennines as result of arc migration driven by sinking of the lithosphere.Tectonics 5, 227-254.
Marinelli, G., 1959. Le intrusioni terziarie dell'Isola d'Elba. Atti Soc. Tosc. Sci. Nat., Mem., Ser. A., 66, 50-253.
Massa, G., Musumeci, G., Mazzarini, F., Pieruccioni, D., 2017. Coexistence of contractional and extensional tectonics during the northern Apennines orogeny: the late Miocene out-of-sequence thrust in the Elba Island nappe stack.Geol. J. 52: 353–368, doi: 10.1002/gj.2761
Mazzarini, F., Musumeci, G., 2008. Hydrofracturing-related sill and dyke emplacement at shallow crustal levels: the Eastern Elba Dyke Complex, Italy. In: Thomson, K., Petford, N. (Eds), Structure and Emplacement of High-level Magmatic Systems. Geological Society: London, Special Publications, 302, 121–129, doi: 10.1144/SP302.9
Mazzarini, F., Musumeci, G., Cruden, A.R., 2011.Vein development during folding in the upper brittle crust: The case of tourmaline-rich veins of eastern Elba Island, northern Tyrrhenian Sea, Italy. Journal of Structural Geology 33, 1509–1522, doi:10.1016/j.jsg.2011.07.001.
Means, W.D., 1983. Microstructure and micromotion in recrystallization flow of Octachloropropane: a first look. Geologische Rundschau 72, 511-528.
Menegon, L., Nasipuri, P., Stünitz, H., Behrens, H. and Ravna, E., 2011. Dry and strong quartz during deformation of the lower crust in the presence of melt. Journal of Geophysical Research: Solid Earth, 116, B10410.
Molli, G., Giorgetti, G., Meccheri, M., 2000.Structural and petrological constraints on the tectono-metamorphic evolution of the Massa Unit (Alpi Apuane, NW Tuscany, Italy).Geological Journal 35, 251-264.
Morgan, S.S., Law, R.D., 2004. Unusual transition in quartzite dislocation creep regimes and crystal slip systems in the aureole of the Eureka Valley-Gioshua Flat-Beer Creek pluton,

California: a case for anhydrous conditions created by decarbonation reactions. Tectonophysics 384, 209–231.

Morgan, S.S., Law, R., de Saint Blanquat, M., 2013. Forceful emplacement of the Eureka Valley–Joshua Flat–Beer Creek composite pluton into a structural basin in eastern California; internal structure and wall rock deformation. Tectonophysics 608, 753–773, doi: 10.1016/j.tecto.2013.08.003.

Morgan, S.S., Nabelek, P.I., Student, J., Sadorski, F., 2016. Fluid-controlled grain boundary migration and switch in slip systems in a high strain, high temperature contact aureole, California, USA. Tectonophysics 676, 42-55.

Musumeci, G., Bocini, L., Corsi, R., 2002. Alpine tectonothermal evolution of the Tuscan Metamorphic Complex in the Larderello geothermal field (northern Apennines Italy).Journal of the Geological Society, London, 159, 443–456.

Musumeci, G., Mazzarini, F., Corti, G., Barsella, M. & Montanari, D. 2005.Magma emplacement in a thrust ramp anticline: The Gavorrano Granite (northern Apennines, Italy). Tectonics, 24, TC6009, doi:10.1029/2005TC001801.

Musumeci, G., Mazzarini, F., Barsella, M., 2008. Pliocene crustal shortening on the Tyrrhenian side of the northern Apennines: evidence from the Gavorrano antiform (southern Tuscany, Italy). Journal of the Geological Society of London 165, 105–114, doi: 10.1144/0016-76492007-004.

Musumeci, G., Mazzarini, F., Tiepolo, M., Di Vincenzo, G., 2011.U-Pb and 40Ar-39Ar geochronology of Palaeozoic units in the northern Apennines: Determining protolith age and Alpine evolution using the Calamita Schist and Ortano Porphyroid. Geological Journal 46, 288–310, doi:10.1002/gj.1266.

Musumeci, G., Vaselli, L., 2012. Neogene deformation and granite emplacement in the metamorphic units of northern Apennines (Italy): Insights from mylonitic marbles in the

Porto Azzurro pluton contact aureole (Elba Island). Geosphere 8(2), 470–490. doi:10.1130/GES00665.1.

Musumeci, G., Mazzarini, F., Cruden, A.R., 2015. The Zuccale Fault, Elba Island, Italy: A new perspective from fault architecture. Tectonics 34. doi: 10.1002/2014TC003809.

Nabelek, P.I., Morgan, S.S., 2012. Metamorphism and fluid flow in the contact aureole of the Eureka Valley–Joshua Flat–Beer Creek (EJB) pluton, California. Geological Society of America Bulletin 124, 228–239.

Pandeli, E., Corti, S., Franceschelli, M., Pecchioni, E., 2001. The varicoloured slates of the Grassera Unit (Central-Eastern Elba Island, Italy): petrographical-mineralogical data and comparisons with other Tuscan and Liguro-Piedmontese Units. Ofioliti 26 (2a), 197-206.

Passchier, C.W., Trouw, A.J., 2005. Microtectonics. Springer-Verlag, Berlin.

Paterson, S.R., Fowler, T.K., 1993. Re-examining pluton emplacement processes. Journal of Structural Geology 15. 191-206.

Paterson, S.R., Tobisch, O.T., 1992. Rates of processes in magmatic arcs: implications for the timing and nature of pluton emplacement and wall rock deformation. Journal of Structural Geology 14, 291–300.

Paterson, S.R. Vernon, R.H., Fowler, T.K. 1991a, Aureole tectonics. In: Derrill, M.K., (Ed.) Contact Metamorphism. Reviews in Mineralogy, Mineralogical Society of America 26, 673-722.

Paterson, S.R. Vernon, R.H., Fowler, T.K., 1991b.Emplacement and deformation of granitoids during volcanic arc construction in the Foothills terrane, central Sierra Nevada, California. Tectonophysics, 191, 89-110.

Pennacchioni, G., Menegon, L., Leiss, B., Nestola, F. and Bromiley, G., 2010. Development of crystallographic preferred orientation and microstructure during plastic deformation of natural coarse-grained quartz veins. Journal of Geophysical Research: Solid Earth, 115

(B12405).

Peretti, F., 2007. I leucograniti del promontorio del Monte Calamita, isola d'Elba. Msc Thesys, Università di Pisa, 155pp.

Pertusati, P. C., Raggi, G., Ricci, C.A., Duranti, S., Palmeri, R., 1993. Evoluzione postcollisionale dell’Elba centro-orientale. Mem. Soc. Geol. Ital. 49, 297–312.

Poirier, J.P., 1985. Creep of crystals: high-temperature deformation processes in metals, ceramics and minerals. Cambridge University Press, Cambridge.

Poirier, J.P., Guillopé, M., 1979.Deformation-induced recrystallization of minerals. Bulletin de Minéralogie 102, 67-74.

Poirier, J.P., Nicolas, A., 1975. Deformation-induced recrystallization by progressive misorientation of subgrain-boundaries, with special reference to mantle peridotites.Journal of Geology 83, 707-720.

Ponziani, F., De Franco, R., Minelli, G., Biella, G., Federico C., Pialli G., 1995. Crustal shortening and duplication of the Moho in the Northern Apennines: a view from the seismic refraction data. Tectonophysics 252, 391–418.

Ramsay, J.G., 1967. Folding and Fracturing of Rocks. McGraw-Hill, New York.

Rosenbaum, G., Lister, G. S., 2004. Neogene and Quaternary rollback evolution of the Tyrrhenian Sea, the Apennines and the Sicilian Maghrebides.Tectonics 23, TC1013, doi:10.1029/2003TC001518.

Rossetti, F., Tecce, F., Billi, A., Brilli, M., 2007. Patterns of fluid flow in the contact aureole of the late Miocene Monte Capanne pluton (Elba Island, Italy): The role of structures and rheology. Contrib. Mineral. Petrol. 153, 743–760, doi: 10.1007/s00410-006-0175-3.

Schmid, S.M., Pfiffner, O.A., Froitzheim, N., Schonborn, G., Kissling, E., 1996. Geophysical geological transect and tectonic evolution of the Swiss-Italian Alps, Tectonics 15, 1036 – 1064.

Selverstone, J., 2005. Preferred embrittlement of graphitic schists during extensional unroofing in the Alps: the effect of fluid composition on rheology in low permeability rocks. J. Metamorph. Geol. 23, 461–470.

Serri, G., Innocenti, F., Manetti, P., 1993.Geochemical and petrological evidence of the subduction of delaminated Adriatic continental lithosphere in the genesis of the Neogene-Quaternary magmatism of central Italy, Tectonophysics 223, 117-147.

Sibson, R.H., 1977. Fault rocks and fault mechanisms. J. Geol. Soc. London 33, 191-213.

Siivola, J., Schmidt, R., 2007. List of mineral abbreviations.Recommendations by the IUGS Subcommission on the systematics of metamorphic rocks. In: Fettes, D. Desmons, J., (Eds.) Metamorphic Rocks: A Classification and Glossary of Terms. Cambridge University Press, Cambridge.

Siniscalchi, A., Diaferia, I., Liuni, M.P., Loddo, M., Magrì, C., Moretti, P., Schiavone, D., Tripaldi, S., 2008. Integrated geophysical approach for imaging the Porto Azzurro (Elba, Italy) pluton and the associated structures. In: Proceedings 33rd International Geological Congress, Oslo, 6-14 August 2008.

Srivastava, P., Mitra, G., 1996. Deformation mechanisms and inverted thermal profile in the North Almora thrust mylonite zone, Kumaon Lesser Himalaya, India. J. Struct. Geol. 18, 27–40.

Stipp, M., Stünitz, H., Heilbronner, R., Schmid S.M., 2002a. The eastern Tonale fault zone: A ‘‘natural laboratory’’ for crystal plastic deformation of quartz over a temperature range from 250 to 700 °C. Journal of Structural Geology 24, 1861 – 1884.

Stipp, M., Stünitz, H., Heilbronner, R., Schmid, S.M., 2002b. Dynamic recrystallization of quartz: Correlation between natural and experimental conditions. In: De Meer, S., Drury, M.R., De Bresser, J.H.P., Pennock, G.M., (Eds.) Deformation Mechanisms, Rheology and Tectonics: Current Status and Future Perspectives. Geol. Soc. Spec. Publ. 200, 171 – 190.

Stipp, M., Fügenschuh, B., Gromet, L.P., Stünitz, H., Schmid, S.M., 2004. Contemporaneous plutonism and strike-slip faulting: A case study from the Tonale fault zone north of the Adamello pluton (Italian Alps). Tectonics 23, TC3004, doi:10.1029/2003TC001515, 2004.

Stipp, M., Tullis, J., Schewath, M., Behmann,J.H., 2010. A new perspective on paleopiezometry: Dinamically recrystallized grain size distribution indicate mechanism changes. Geology, 38, 759-762, doi: 10.1130/G31162.1

Theye, T., Reinhard, T.J., Goffé, B., Jolivet, L., 1997. Ferro- and magnesio-carpholite from the Monte Argentario (Italy): first evidence for high-pressure metamorphism of the metasedimentary Verrucano sequence, and significance for P-T path reconstruction. European Journal of Mineralogy 9, 859-873.

Trepmann, C. A., Hsu, C., Hentschel, F., Döhler, K., Schneider, C., Wichmann, V., 2017. Recrystallization of quartz after low-temperature plasticity–The record of stress relaxation below the seismogenic zone. Journal of Structural Geology 95, 77-92.

Urai, J.L., 1983. Water assisted dynamic recrystallization and weakening in polycrystalline bischofite. Tectonophysics 96, 125-157.

Urai, J.L., Means, W.D., Lister, G.S., 1986. Dynamic recrystallization of minerals. In: Heard, H.C., Hobbs, B.E., (Eds.) Mineral and rock deformation: laboratory studies, the Paterson volume. Geophys. Monogr. 36, 161-200. American Geophysical Union, Washington D.C.

Voll, G., 1976. Recrystallization of quartz, biotite and feldspars from Erstfeld to the Leventina Nappe, Swiss Alps, and its geological significance. Schweizerische mineralogische und petrographische Mitteilungen 56, p.147.

Westerman, D.S., Dini, A., Innocenti, F., Rocchi, S., 2004. Rise and fall of a nested Christmas-tree laccolith complex, Elba Island, Italy In: Breitkreuz, C., Petford, N., (Eds.) Physical Geology of High-Level Magmatic Systems.Geol. Soc. London Spec. Publ. 234, 195–213.

990

Figure captions

Fig. 1 – **a)** Tectonic sketch map of the northern Apennines and Alpine Corsica (modified after Bonini et al., 2014). MTR: Mid-Tuscan Ridge; AA: Alpi Apuane massif; MP: Monti Pisani massif; MR: Monticiano-Roccastrada massif; LGF: Larderello geothermal field; G: Gavorrano pluton; **b)** Tectonic sketch map of the Elba Island (modified after Massa et al., 2017).

Fig. 2 – Geological sketch map of the Calamita Promontory (modified after Musumeci et al., 2015). CNT: Capo Norsi Thrust; FSZ: Felciaio Shear Zone; CSZ: Calanchiole Shear Zone; ZF: Zuccale Fault. See text for further details.

Fig. 3 – Tectonic sketch map of the Calamita Unit showing the distribution of the main structural elements, low- and-high strain domains, ductile and brittle structures (see text for further details). Structural elements are plotted on equal area, lower hemisphere stereographic projections. The foliation pattern highlights the presence of an upright antiform refolding the regional foliation (Ripalte Antiform). Lineations are constantly oriented E-W, similarly to brittle slickenlines. The sense of shear is constantly top-to-the E.

Fig. 4 – Sketch map showing the distribution of high- and low-strain domains in a key area (Pontimento Area; location in Fig. S1 in supplementary material): **a**) Detail of sector B (Fig. 3), displaying two decametric high-strain domains surrounded by domains of relatively low strain. Note the local presence of foliated dykes caught within high-strain zones; **b**) Detail of a low-strain domain area characterized by east-verging tight folds developed in quartz-rich layers with SpL axial plane foliation; **c**) Detail of continuous penetrative SpH foliation within

a high-strain domain. Note that SpL and SpH foliations are sub-parallel.

Fig. 5 –**a**) Detail of mesoscale strain partitioning with well-foliated high-strain domains (HSD) and relatively coarse-grained low-strain domains (LSD). Location of Pontimento Area is in Fig. S1. Mineral abbreviations are from Siivola and Schmid (2007); **b**) HSD: mylonitic schists characterized by asymmetric boudinage and sigmoidal Qtz-lenses indicating top-to-the-east sense of shear (Praticciolo area, location in Fig. S1); **c)** HSD: Qtz-Wmca-Bt aggregate lineations and And-Crd mineral lineations directed E-W on a SpH foliation surface (Remaiolo area, location in Fig. S1); **d**) S-C' fabric developed in mylonitic And-Crd schists indicating top-to-the-e sense of shear (Praticciolo area, location in Fig. S1); **e**) YZ-section (N-S; perpendicular to LpH) of a sheath fold system exposed in the Calanchiole marble at Punta Rossa area, location in Fig. S1; **f**) Mesoscale duplexing of sheath folds in the Calanchiole marble indicating top-to-the-east sense of shear (Punta Rossa area, location in Fig. S1).

Fig. 6 – Microphotographs of low strain domains taken under cross polarised light (abbreviations from Siivola and Schmid, 2007): **a)** Detail of the SpL foliation, characterized by the sub-parallel arrangement of mica- and Qtz-rich domains; **b)** Very coarse-grained aggregates of misoriented And and Crd grains embedded in a fine-grained Wmca-Bt rich matrix; **c)** Microfabric characterized by coarse-grained Qtz- and Bt-domains defining the SpL with associated subparallel And-grains. Note the interlobate to amoeboid textures in Qtz; **d)** Microstructure displaying subparallel Qtz-domains with interlobate fabric bound by very thin Bt-Wmca bands.

Fig. 7 – Microstructures in high strain domains from Praticciolo section (see location in Fig. S1; abbreviations from Siivola and Schmid, 2007): **a**) Example of stage 1 microfabric taken at

cross polarised light from a Bt-Crd-And mylonitic schist characterized by amoeboid quartz grains enveloping Bt-grains and showing a well developed lattice preferred orientation; **b**) Example of stage 2 microfabric taken at cross polarised light in a mylonitic Wmca-Bt-Crd-And schist. A coarse, old grain, is surrounded by a mantle of finely-recrystallized stage 2 grains elongated parallel to the SpH (detail in Fig. 9c); **c**) Example, taken at cross polarised light, of a microfabric with coarse-grained stage 1 quartz overprinted by very fine-grained stage 3 quartz localized in small-scale shear fractures (see detail in Fig. 10b, c) in a sample of Chl-Wmca-Crd-And mylonite; **d**) Synkinematic Crd porphyroblast in a Bt-Crd-And schist. Note the deflected internal foliation and strain caps wrapping the crystal (cross polarised light); **e**) S-C' fabric in a Crd-And mylonite. Note the deflection of the SpH (S) surfaces along east-dipping C' shear planes with top-to-the-east sense of shear (plane polarised light); **f**) Pinitized Crd porphyroblasts in a Wmca-Bt-Crd-And in schist with sigmoidal shape indicating top to east sense of shear (plane polarised light);

Fig. 8–Images of stage 1 microfabric, taken under cross polarised light (mineral abbreviations from Siivola and Schmid, 2007): **a)** Interlobate coarse-grained Qtz within a Crd-And-Bt mylonitic schist. Note the isolated tiny grains embedded in coarser grains (island grains); **b)** Detail of a quartz layer in a folded quartzite lens embedded in a Bt-Crd-And schist. Note the coarse-grained Qtz grains with interlobate boundaries intersecting at roughly 90 degrees (reticular structure) and internal undulose extinction; **c)** Detail of a local polygonal fabric (red arrow) witnessed in a Qtz-layer within a Bt-Crd-And schist; **d)** Detail of an amoeboid quartz fabric from a Bt-Crd-And schist showing tiny island grains in optical continuity with coarser grains (left-over grains). Red arrows marks the grains in optical continuity; **e)** Detail of Fig. 7a showing the amoeboid Qtz fabric bound by subparallel Bt grains. Red arrow indicates a window microstructure, where Bt is not present and two adjacent Qtz grains produce an

interlobate boundary. Note also the pinning of Qtz around Bt (blue arrow); **f**) Amoeboid Qtz fabric with island grains from a sample of Bt-Wmca-And-Crd. Note the widespread presence of subgrain boundaries.

Fig. 9– Images of stage 2 microfabric, taken at cross polarised light (Mineral abbreviations from Siivola and Schmid, 2007): **a**) Stage 2 microfabric characterized by roughly 100 µm-sized grains with a shape preferred orientation. Note the presence of an old grain on the right with internal subgrains, similar in shape and size to stage 2 grains. Image taken in a Wmca-Bt-And-Crd bearing quartzite; **b**) Detail of stage 2 grains localized along interlobate grain boundaries between stage 1 grains in a Wmca-bearing quartzite. Red arrow indicates a subgrain showing the same size of stage 2 grains; **c**) Detail of Fig. 7b showing a ribbon of stage 2 grains in a mylonitic Wmca-Bt-Crd-And schist. The ribbon consists of subgrains and new grains with similar grain size and displaying a shape preferred orientation subparallel to the SpH, defined by subparallel Wmca grains; **d)** Detail of the sample displayed in Fig. 7a with stage 2 grains localized in the strain cap of sericitized And porphyroblast. Note the deflection of the SpH foliation, defined by Bt-grains, in the strain cap and the transition to stage 1 microfabric away from the strain cap; **e**) Sample of a microfold affecting quartz layers in a Wmca-And-Crd bearing quartzite. Note the presence of alternating layers of coarse and fine-grained quartz and isolated old grains in a very fine quartz matrix; **f)** Detail of the hinge zone of the fold in Fig. 9e showing elongated stage 2 grains localized along interlobate grain boundaries between stage 1 grains. Note that the preferred orientation of stage 2 grains defines the axial plane foliation of the fold.

Fig. 10– Microphotographs of stage 3 microfabric taken at cross polarised light (mineral abbreviations from Siivola and Schmid, 2007): **a**) Detail of stage 3 microfabric bounding the

cataclastic band from the sample in Fig. 11d. Stage 3 grains occur as tiny interlobate aggregates and bulges around coarser stage 1 and 2 grains; **b**) Set of conjugate dextral (on the left) and sinistral (on the right) shear fractures in coarse grained stage 1 quartz (detail of the structures visible in Fig. 7c). Shear fractures are decorated by tiny stage 3 grains (detail in Fig. 10c). Grains on the bottom of the image represent stage 2 grains mantling stage 1 grains; **c**) Detail of the stage 3 grains of Fig. 10b. Note that stage 3 grains exhibit a shape preferred orientation defining an oblique foliation in respect to the boundaries of the shear fracture concordant with the local dextral sense-of-shear; **d**) Cataclastic quartzite showing recrystallized sets of perpendicular fractures within an old grain decorated with misoriented stage 3 grains.

Fig. 11 – Brittle deformation structures from the Praticciolo area (see location in Fig. S1): **a)** Overview of an high-strain domain of brittle deformation characterized by low angle Y-shears associated with centimetric cataclastic bands (white arrow), moderately dipping R-shears and high angle R’ shears cross-cutting the SpH foliation. See text for further details; **b)** Stereographic projection (equal area, lower hemisphere) of the poles of the faults depicted in Fig. 11a; **c**) Detail of the core zone of an Y-shear zone. Note the cataclastic fabric cross-cutting the SpH foliation and the presence of a layer of ultracataclasite in correspondence of the contact with the hanging-wall block. Black rectangle indicates the position of the thin section of Fig. 11d; **d**) Microphotograph taken under cross polarised light showing the transition from foliated quartzite (left side of photo) to ultracataclasite (right side of photo). Note in the centre the millimetre-thick area bounded by dashed white lines characterized by stage 3 quartz grains. See text for further explanations.

Fig. 12 – Conceptual model explaining the development of stage 1 (Grain Boundary Migration; GBM), 2 (Subgrain Rotation; SGR) and 3 (Bulging; BLG) microfabrics within high-strain domains. Deformation at peak metamorphic conditions is recorded by GBM-recrystallization in quartz. During aureole cooling, SGR recrystallization overprints old GBM grains producing ribbons and core-and-mantle structures. At lower temperatures GBM and SGR-microfabrics are in turn affected by BLG-recrystallization and brittle cataclasis. See text for further details. *: peak temperature from Duranti et al. (1992); **: brittle-ductile transition for quartz after Voll (1976).

Fig. 13– Block diagram illustrating the reconstructed architecture of the metamorphic units (Calamita Schist and Ortano units) hosting the Porto Azzurro pluton. The Ripalte antiform in the eastern coast is interpreted as the hanging-wall anticline of an inferred buried thrust at the base of pluton. See text for further details.

Supplementary material

Supplementary figure 1 –Schematic geological-structural map reporting the position of meso- and microscale fabric shown in Figs. 4, 5, 7, 11.

Supplementary table 1 – Table of representative samples listing: sample, locality, GPS coordinates, mineral assemblage, lithology and fabric description. Mineral abbreviations are from Siivola and Schmid (2007). LSD: Low-strain domains; HSD: High-strain domains.

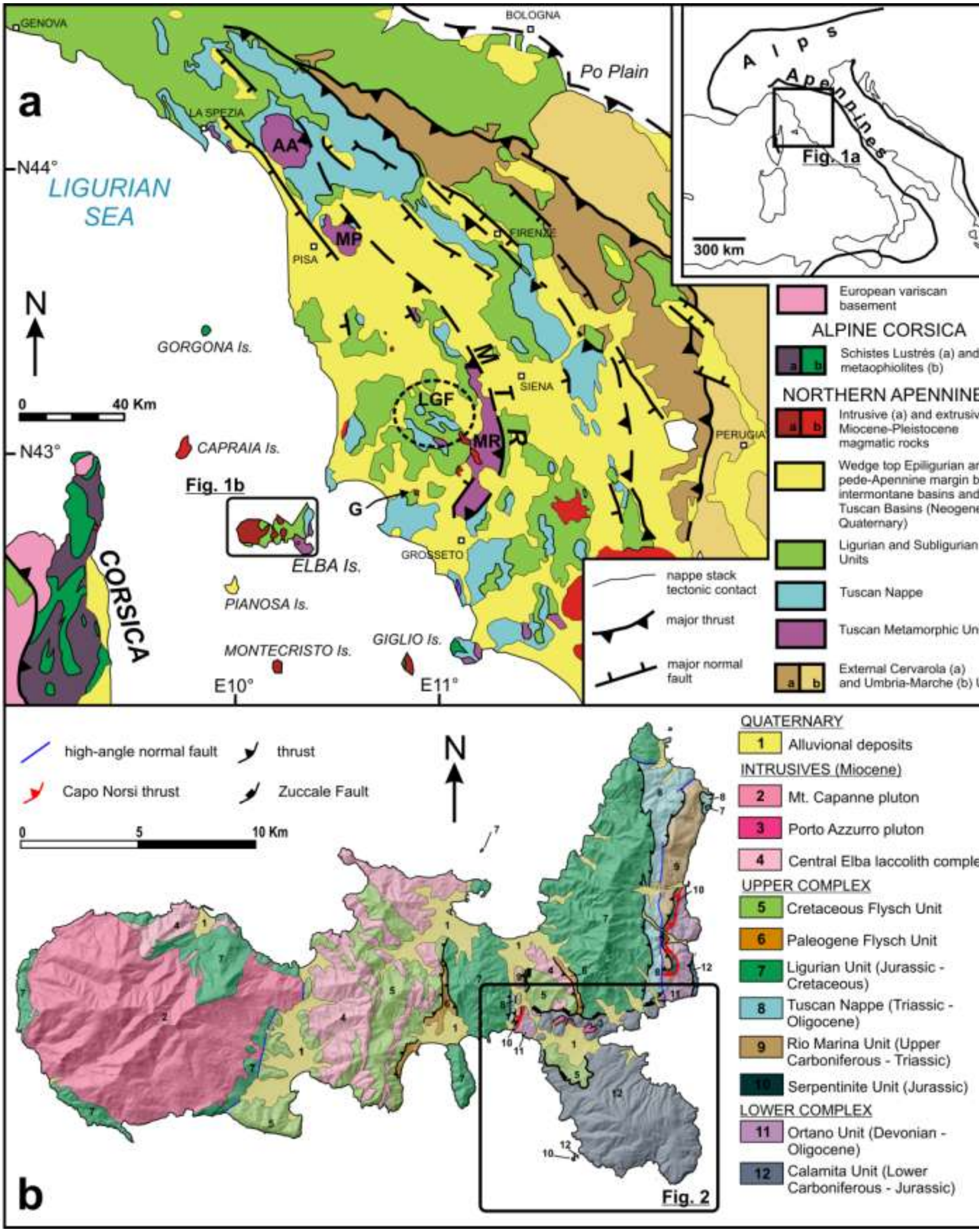
a
b
GENOVA
BOLOGNA
Po Plain
LA SPEZIA
AA
N44°
LIGURIAN SEA
MP
PISA
FIRENZE
N
0 40 Km
GORGONA Is.
SIENA
M T R
LGF
MR
N43°
CAPRAIA Is.
PERUGIA
Fig. 1b
G
ELBA Is.
GROSSETO
CORSICA
PIANOSA Is.
MONTECRISTO Is.
GIGLIO Is.
E10°
E11°
Alps
Apennines
Fig. 1a
300 km
European variscan basement
ALPINE CORSICA
Schistes Lustrès (a) and metaophiolites (b)
NORTHERN APENNINE
Intrusive (a) and extrusive Miocene-Pleistocene magmatic rocks
Ligurian and Subligurian Units
Tuscan Nappe
Tuscan Metamorphic Un
nappe stack tectonic contact
major thrust
major normal fault
high-angle normal fault
thrust
Capo Norsi thrust
Zuccale Fault
0 5 10 Km
QUATERNARY
1 Alluvional deposits
INTRUSIVES (Miocene)
2 Mt. Capanne pluton
3 Porto Azzurro pluton
UPPER COMPLEX
5 Cretaceous Flysch Unit
6 Paleogene Flysch Unit
7 Ligurian Unit (Jurassic - Cretaceous)
8 Tuscan Nappe (Triassic - Oligocene)
9 Rio Marina Unit (Upper Carboniferous - Triassic)
10 Serpentinite Unit (Jurassic)
LOWER COMPLEX
11 Ortano Unit (Devonian - Oligocene)
12 Calamita Unit (Lower Carboniferous - Jurassic)
Fig. 2

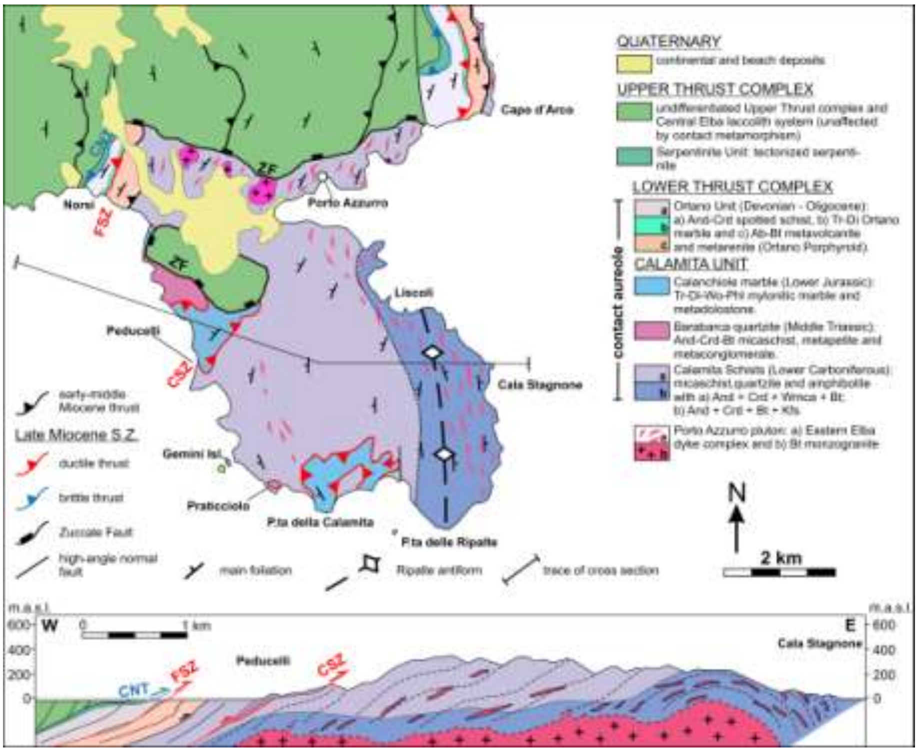
Capo d'Arco
Norsi
FSZ
CNT
ZF
Porto Azzurro
Liscoli
Peducelli
CSZ
Cala Stagnone
Gemini Isl.
Praticciolo
P.ta della Calamita
P.ta delle Ripalte
QUATERNARY
continental and beach deposits
UPPER THRUST COMPLEX
undifferentiated Upper Thrust complex and Central Elba laccolith system (unaffected by contact metamorphism)
Serpentinite Unit: tectonized serpentinite
LOWER THRUST COMPLEX
Ortano Unit (Devonian - Oligocene): a) And-Crd spotted schist, b) Tr-Di Ortano marble and c) Ab-Bt metavolcanite and metarenite (Ortano Porphyroid).
CALAMITA UNIT
Calanchiole marble (Lower Jurassic): Tr-Di-Wo-Phl mylonitic marble and metadolostone.
Barabarca quartzite (Middle Triassic): And-Crd-Bt micaschist, metapelite and metaconglomerate.
Calamita Schists (Lower Carboniferous): micaschist,quartzite and amphibolite with a) And + Crd + Wmca + Bt; b) And + Crd + Bt + Kfs.
Porto Azzurro pluton: a) Eastern Elba dyke complex and b) Bt monzogranite
contact aureole
N
2 km
early-middle Miocene thrust
Late Miocene S.Z.
ductile thrust
brittle thrust
Zuccale Fault
high-angle normal fault
main foliation
Ripalte antiform
trace of cross section
m.a.s.l.
W
E
0
1 km
600
400
200
Peducelli
Cala Stagnone

Figure 1

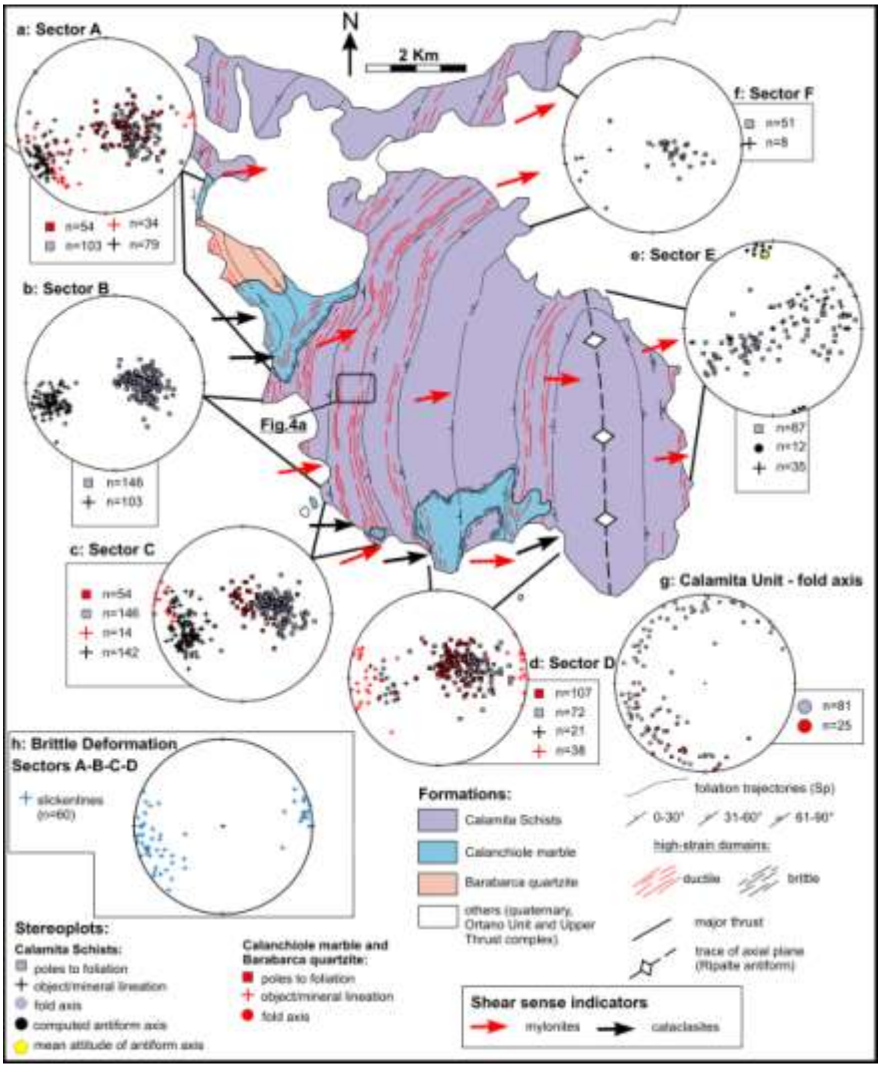
a: Sector A
b: Sector B
c: Sector C
d: Sector D
e: Sector E
f: Sector F
g: Calamita Unit - fold axis
h: Brittle Deformation
Sectors A-B-C-D
N
2 Km
Fig.4a
Formations:
Calamita Schists
Calanchiole marble
Barabarca quartzite
others (quaternary, Ortano Unit and Upper Thrust complex)
foliation trajectories (Sp)
high-strain domains:
ductile
brittle
major thrust
trace of axial plane (Ripalte antiform)
Stereoplots:
Calamita Schists:
poles to foliation
object/mineral lineation
fold axis
computed antiform axis
mean attitude of antiform axis
Calanchiole marble and Barabarca quartzite:
poles to foliation
object/mineral lineation
fold axis
Shear sense indicators
mylonites
cataclasites

Figure 2

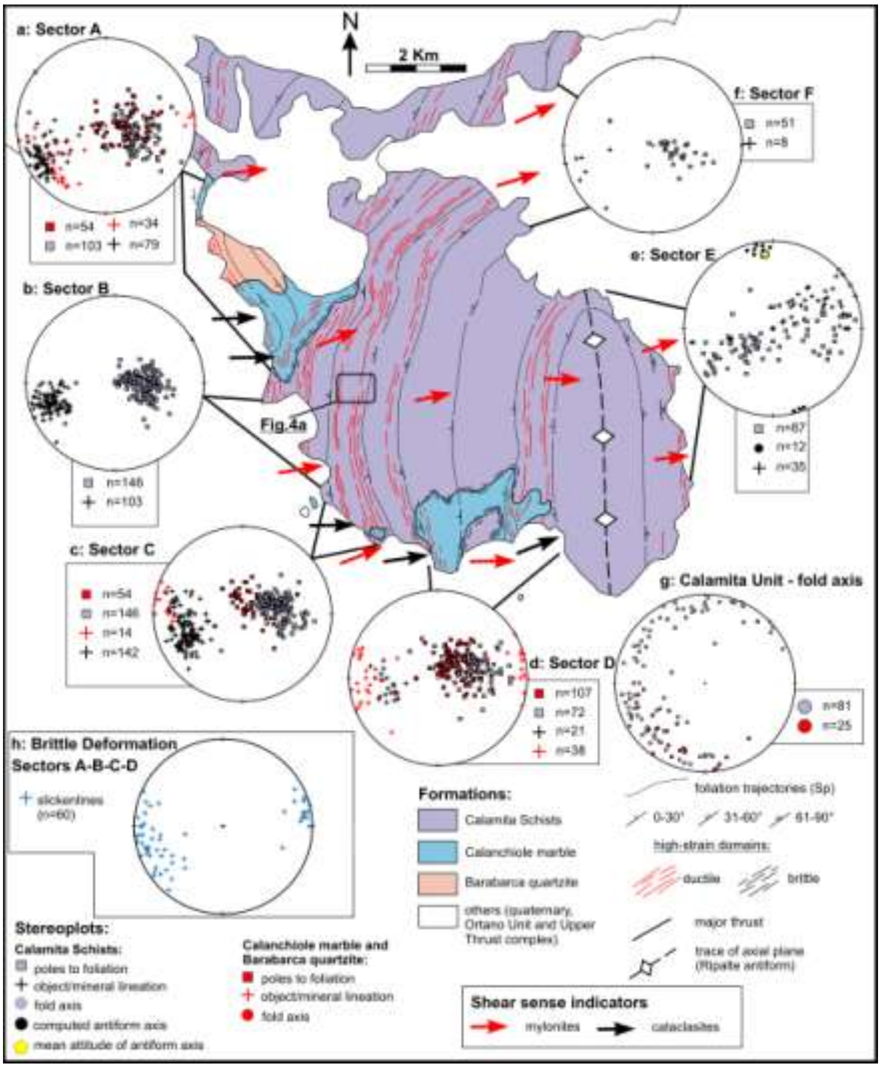

a: Sector A
n=54
n=34
n=103
n=79
b: Sector B
n=146
n=103
c: Sector C
n=54
n=146
n=14
n=142
d: Sector D
n=107
n=72
n=21
n=38
e: Sector E
n=67
n=12
n=35
f: Sector F
n=51
n=8
g: Calamita Unit - fold axis
n=81
n=25
h: Brittle Deformation
Sectors A-B-C-D
slickenlines
(n=60)
N
2 Km
Fig.4a
Formations:
Calamita Schists
Calanchiole marble
Barabarca quartzite
others (quaternary, Ortano Unit and Upper Thrust complex)
foliation trajectories (Sp)
0-30°
31-60°
61-90°
high-strain domains:
ductile
brittle
major thrust
trace of axial plane
(Ripalte antiform)
Stereoplots:
Calamita Schists:
poles to foliation
object/mineral lineation
fold axis
computed antiform axis
mean attitude of antiform axis
Calanchiole marble and
Barabarca quartzite:
poles to foliation
object/mineral lineation
fold axis
Shear sense indicators
mylonites
cataclasites

Figure 3

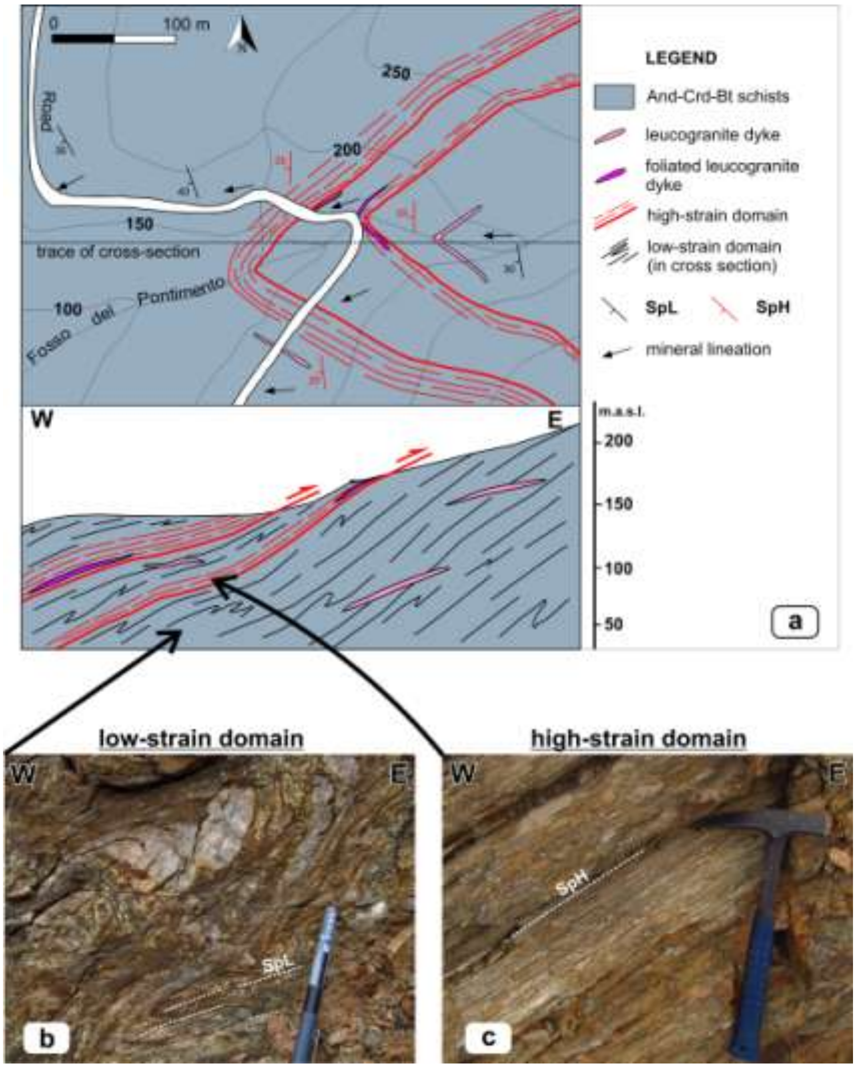
0
100 m
N
LEGEND
And-Crd-Bt schists
leucogranite dyke
foliated leucogranite dyke
high-strain domain
low-strain domain (in cross section)
SpL
SpH
mineral lineation
250
200
150
100
Road
trace of cross-section
Fosso del Pontimento
W
E
m.a.s.l.
200
150
100
50
a
low-strain domain
high-strain domain
SpL
SpH
b
c

Figure 4

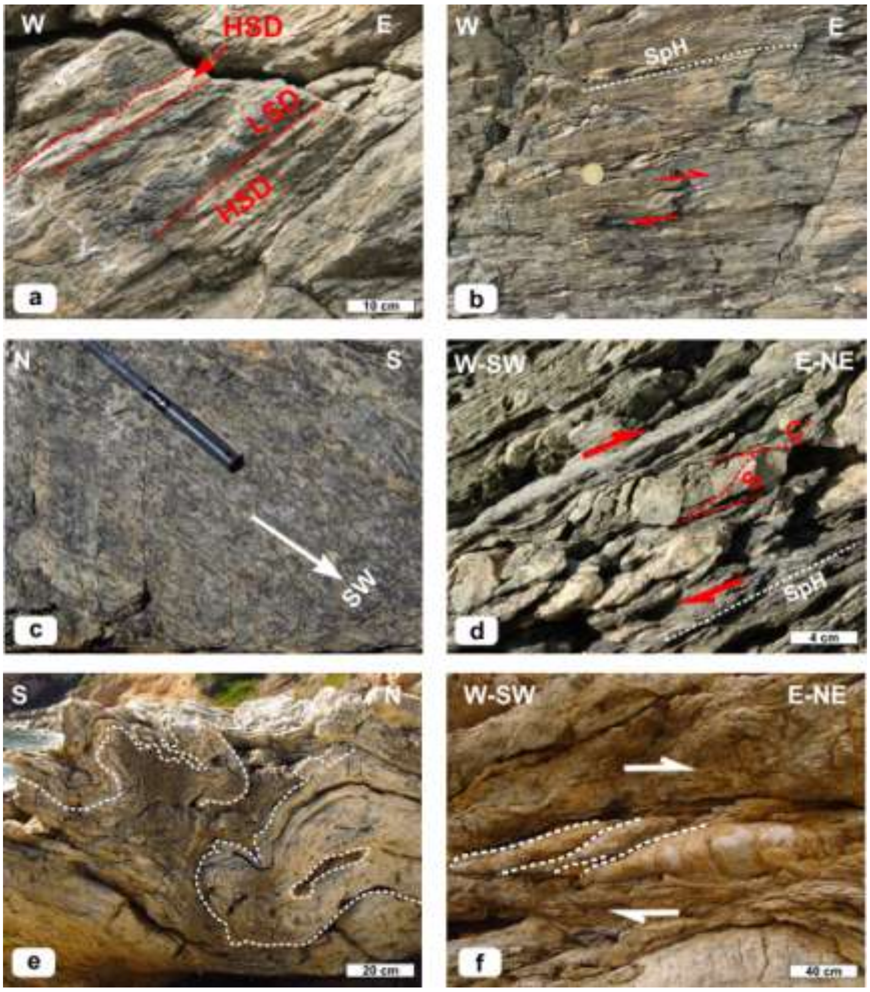
W
E
HSD
LSD
HSD
a
10 cm
W
E
SpH
b
N
S
SW
c
W-SW
E-NE
C
S
SpH
d
4 cm
S
N
e
20 cm
W-SW
E-NE
f
40 cm

Figure 5

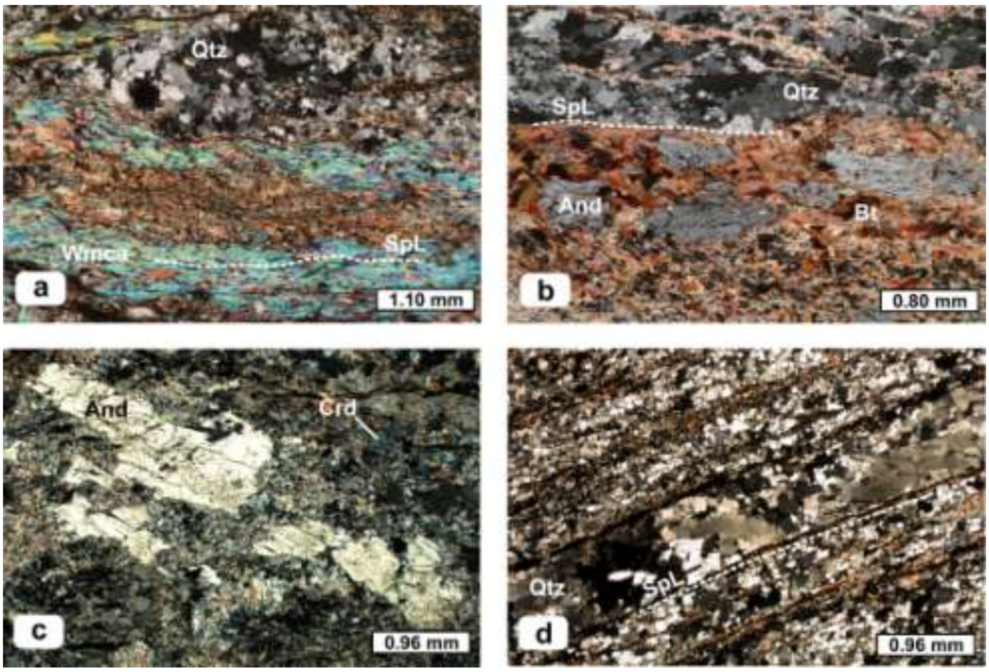
Qtz
Wmca
SpL
a
1.10 mm
SpL
Qtz
And
Bt
b
0.80 mm
And
Crd
c
0.96 mm
Qtz
SpL
d
0.96 mm

Figure 6

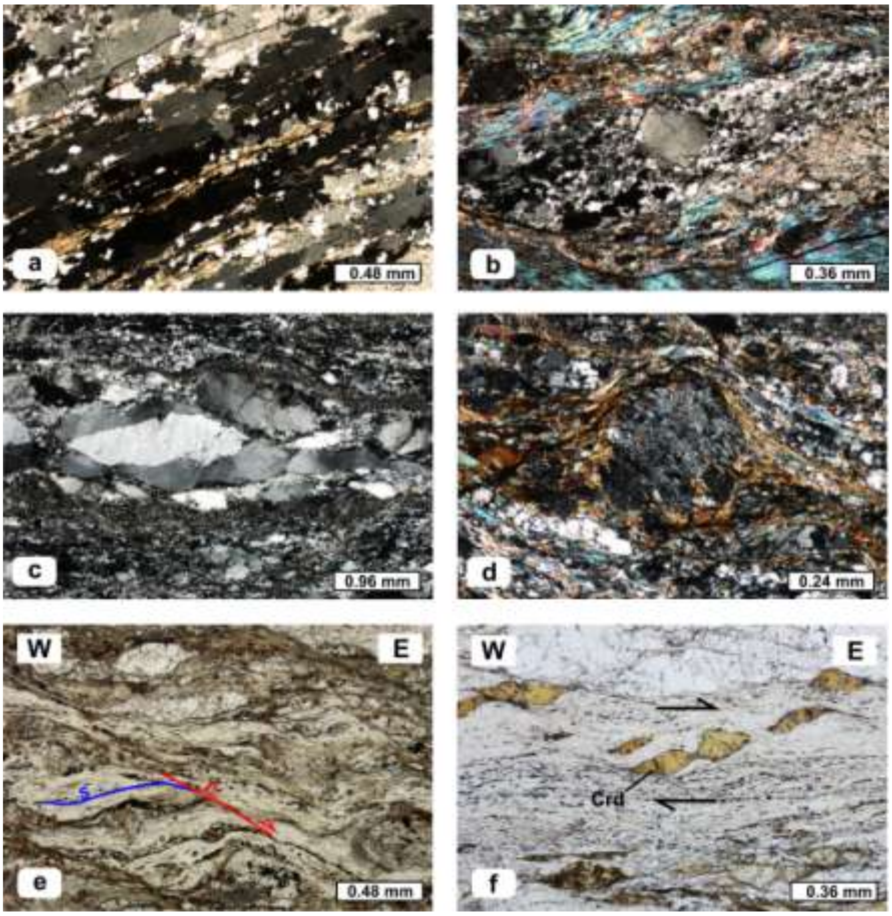

Figure 7

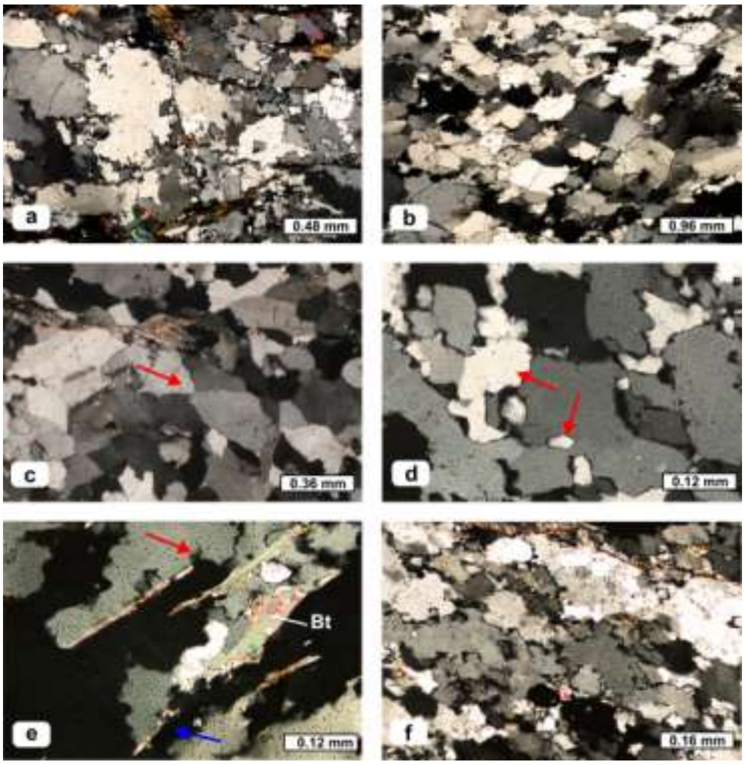

Figure 8

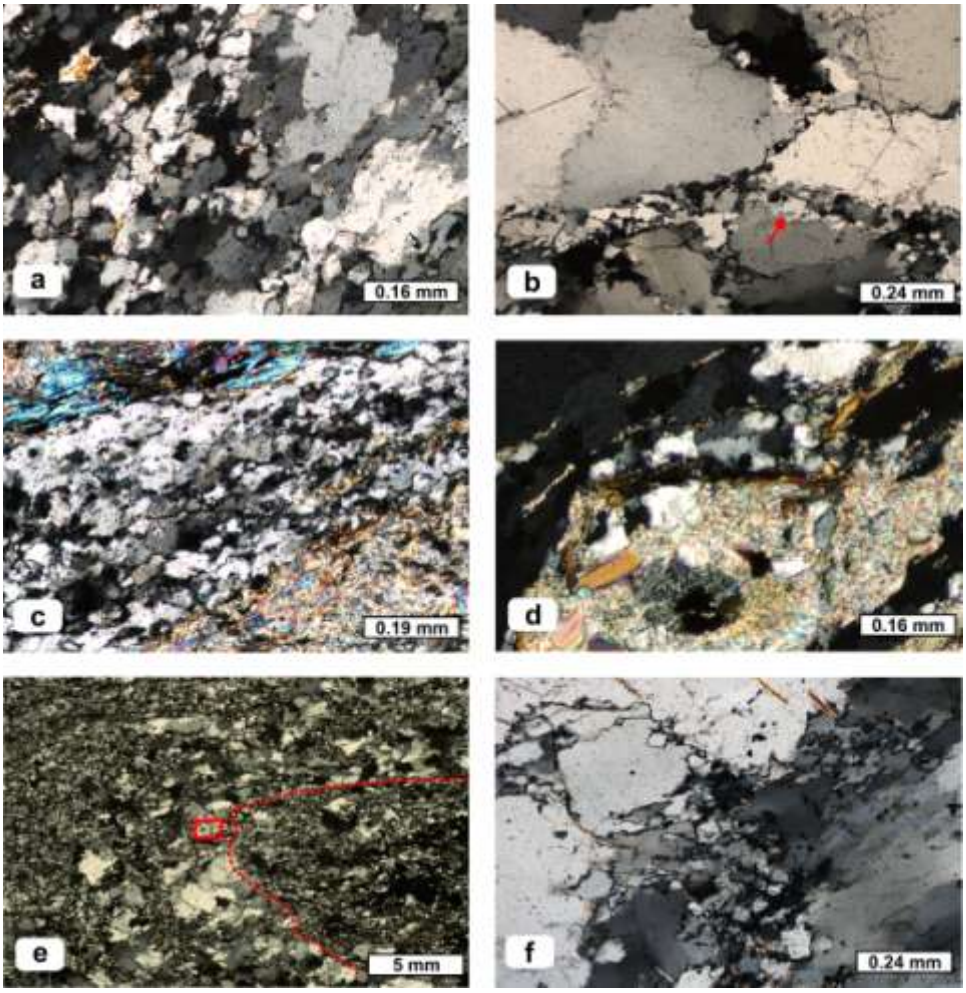

Figure 9

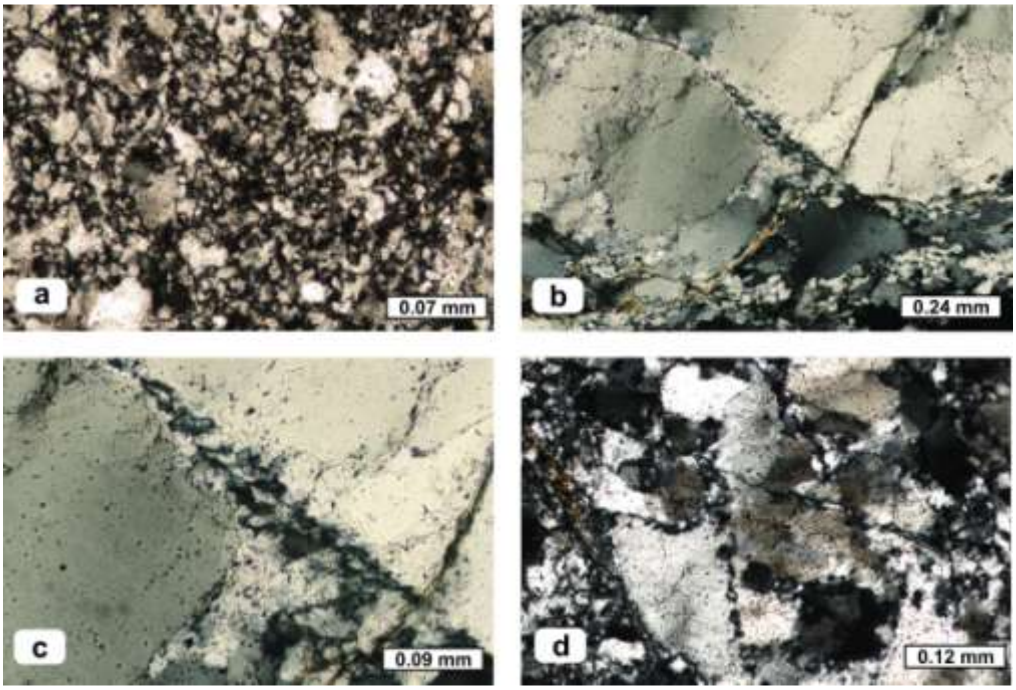

Figure 10

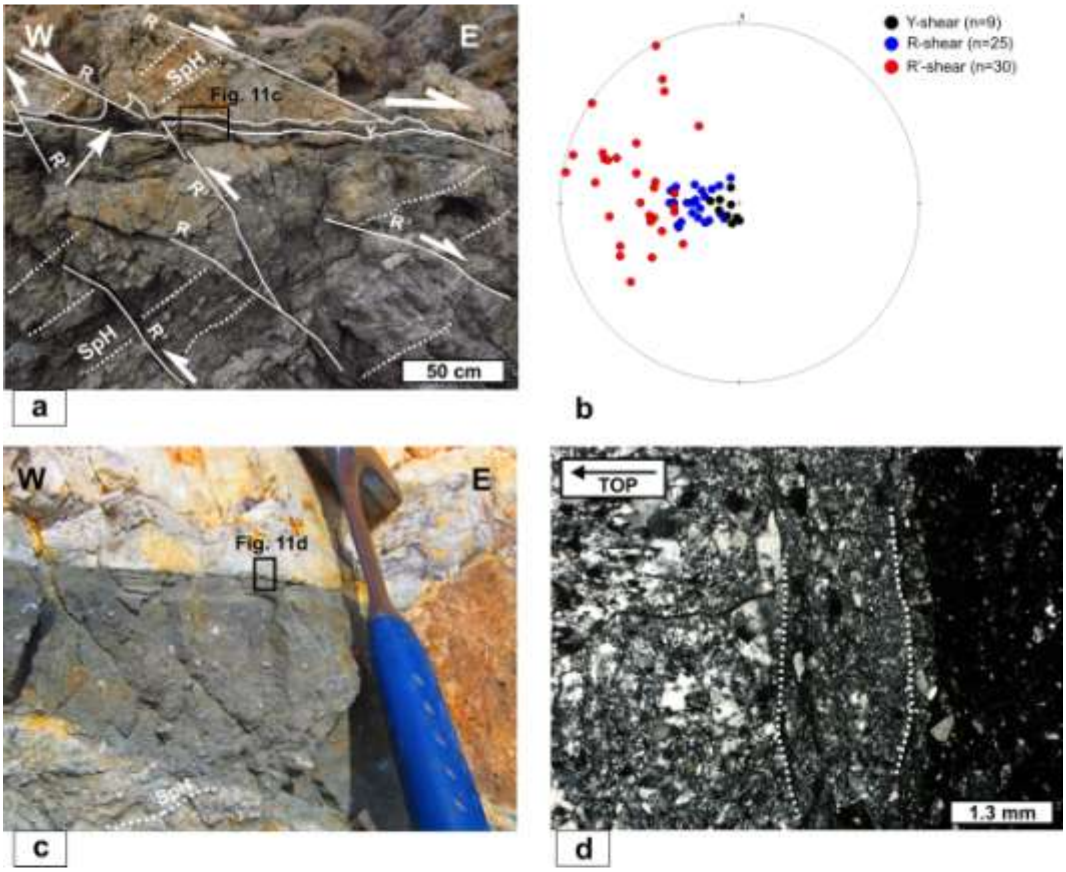

Figure 11

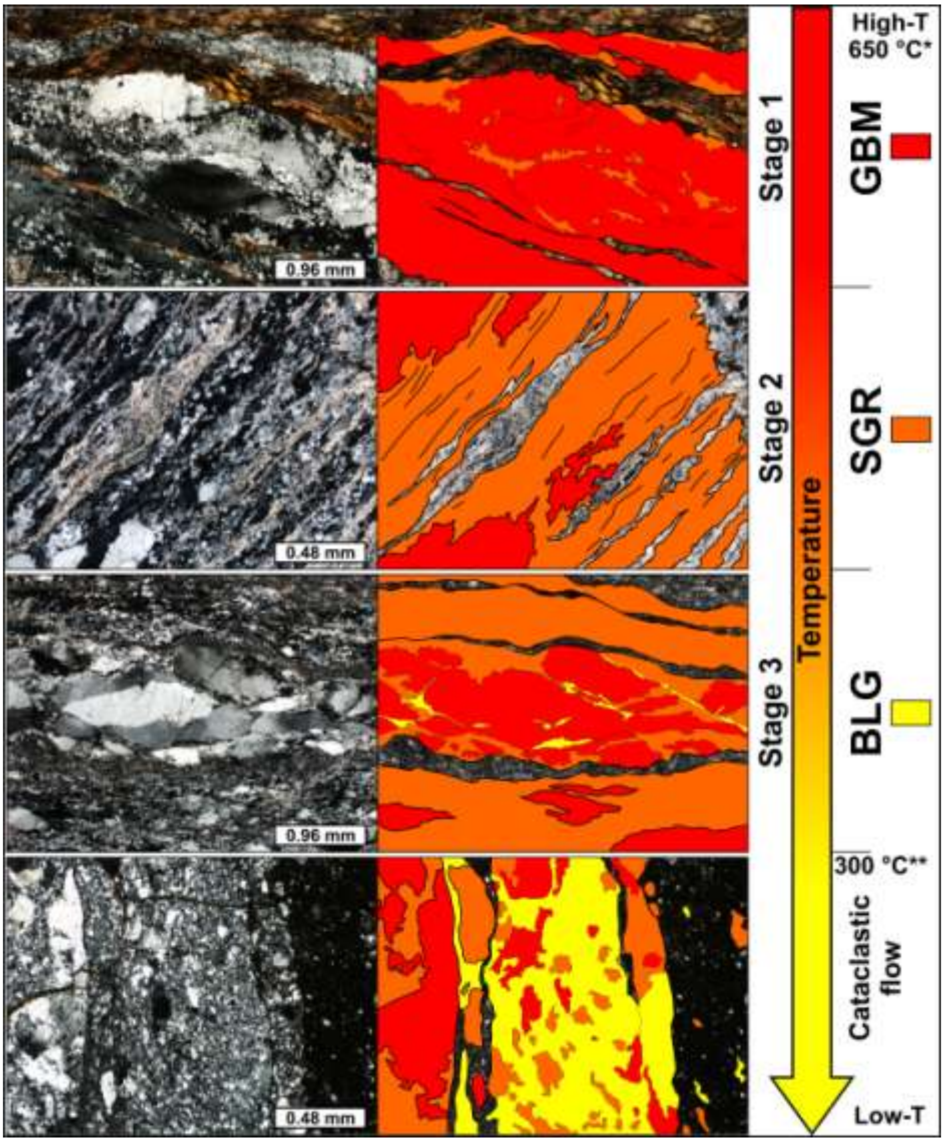

High-T
650 °C*
GBM
SGR
BLG
300 °C**
Cataclastic flow
Low-T
Stage 1
Stage 2
Stage 3
Temperature
0.96 mm
0.48 mm
0.96 mm
0.48 mm

Figure 12

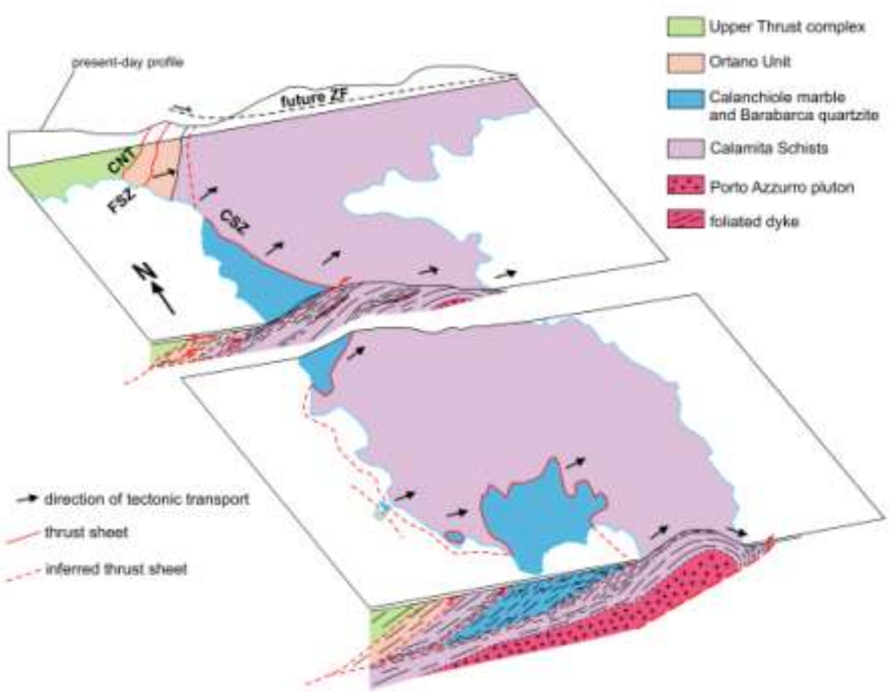
Upper Thrust complex
Ortano Unit
Calanchiole marble
and Barabarca quartzite
Calamita Schists
Porto Azzurro pluton
foliated dyke
present-day profile
future ZF
CNT
FSZ
CSZ
N
direction of tectonic transport
thrust sheet
inferred thrust sheet

Figure 13